Homogeneous bubble nucleation in rhyolitic magmas: An experimental study of the effect of H_2O and CO_2

C. C. Mourtada-Bonnefoi and D. Laporte

Laboratoire Magmas et Volcans, CNRS, Université Blaise Pascal, Observatoire de Physique du Globe de Clermont-Ferrand, Clermont-Ferrand, France

Received 20 June 2000; revised 31 January 2001; accepted 20 August 2001; published 13 April 2002.

[1] Rapid decompression experiments were performed to study homogeneous bubble nucleation in a crystal-free rhyolitic liquid at 800°C. Bubble nucleation was produced by lowering the pressure at 1–10 MPa s^{-1} from an initial value between 200 and 295 MPa to a final value below the volatile saturation pressure P_{Sat}. Six volatile compositions with 4.1–7.7 wt % H_2O and 10–1200 ppm CO_2 were investigated. For each composition we determined the critical pressure P_{HoN} below which homogeneous nucleation can proceed. The samples quenched below P_{HoN} showed a nucleated core with a large number of uniformly spaced bubbles. With decreasing pressure, bubble number densities increased from $<10^{11}$ m^{-3} (for samples quenched just below P_{HoN}) to $>10^{15}$ m^{-3}. The degree of supersaturation required for homogeneous nucleation, ΔP_{HoN} (= $P_{Sat} - P_{HoN}$), increased with decreasing H_2O content or increasing CO_2 content. Huge values of ΔP_{HoN}, $\geq$135 to 310 MPa, were measured in the H_2O-poor compositions (4.1–4.6 wt % H_2O; 50–1100 ppm CO_2); much lower values from $\approx$60 to 160 MPa were obtained in the H_2O-rich compositions (7.0–7.7 wt % H_2O; 10–630 ppm CO_2). The high ΔP_{HoN} in liquids with 4–5 wt % H_2O should result in the buildup of large degrees of supersaturation during magma ascent, a very late nucleation event, and a rapid (explosive) vesiculation. By contrast, rhyolitic liquids with much larger water contents have higher saturation pressures and much lower ΔP_{HoN}: bubble nucleation may therefore occur at depth in the volcanic conduit favoring a subsequent near-equilibrium degassing. *INDEX TERMS:* 1749 History of Geophysics: Volcanology, geochemistry, and petrology; 8414 Volcanology: Eruption mechanisms; 8045 Structural Geology: Role of fluids; *KEYWORDS:* volcanology, eruption mechanisms, degassing, bubble nucleation, felsic magmas, explosive volcanism

1. Introduction

[2] Felsic magmas cause the most powerful explosive eruptions at the Earth's surface mainly by decompression-driven exsolution of magmatic volatiles. They come from magma chambers at lithostatic pressures of up to 450 MPa and may contain high amounts of dissolved volatiles among which water and carbon dioxide are the most abundant and range from 3 to 10 wt % and up to 1000 ppm, respectively [*Johnson et al.*, 1994; *Anderson et al.*, 1989; *Bacon et al.*, 1992; *Wallace and Gerlach*, 1994; *Wallace et al.*, 1995; *Lowenstern*, 1994; *Lowenstern et al.*, 1997; *Barclay et al.*, 1996, 1998; *Martel et al.*, 1998]. The dynamics of magma ascent from the chamber to the vent are known to be mainly controlled by vesiculation processes [*Jaupart*, 1996; *Woods*, 1995], which are affected by the kinetics of bubble nucleation. A major aspect of bubble nucleation is that it requires a certain degree of volatile supersaturation to proceed, this degree being maximum in the case of homogeneous bubble nucleation and lower in the case of heterogeneous nucleation on crystals [*Hurwitz and Navon*, 1994; *Mourtada-Bonnefoi*, 1998; *Mourtada-Bonnefoi and Laporte*, 1999; *Gardner et al.*, 1999; *Mangan and Sisson*, 2000]. Both theoretical and previous experimental studies [*Hirth et al.*, 1970; *Sparks*, 1978; *Bottinga and Javoy*, 1990; *Debenedetti*, 1996; *Hurwitz and Navon*, 1994; *Mourtada-Bonnefoi*, 1998; *Mourtada-Bonnefoi and Laporte*, 1999; *Gardner et al.*, 1999; *Mangan and Sisson*, 2000] indicate that the difference between the volatile saturation pressure and the pressure at which homogeneous bubble nucleation proceeds, ΔP_{HoN}, is very large and ranges from 60 to 300 MPa. Nucleation also controls vesiculation dynamics through the number density of nuclei as this number determines the length scale of diffusion to growing bubbles [*Proussevitch and Sahagian*, 1996, 1998]. Data on nucleation rates and nucleation densities remain very scarce [*Klug and Cashman*, 1994; *Mangan and Cashman*, 1996; *Navon and Lyakhovsky*, 1998]. We carried out a series of decompression experiments to characterize the effect of water and carbon dioxide on the kinetics of homogeneous bubble nucleation in rhyolitic magmas. We were able to determine the nucleation pressures and the main textural parameters (bubble number density and bubble size distribution) for six different volatile compositions with 4.1–7.7 wt % water and up to 1200 ppm carbon dioxide.

0148-0227/02/2001JB000290$09.00

2. Experimental and Analytical Techniques

2.1. Starting Glasses

[3] The starting glasses for homogeneous bubble nucleation experiments must satisfy two fundamental conditions. First, they must not contain bubbles: the diffusive growth of these bubbles during the decompression and nucleation steps will indeed decrease the volatile content in the neighboring liquid and therefore alter its capacity to nucleate bubbles. In particular, hydrous rhyolitic glasses prepared from powders (e.g., powdered obsidian) contain a high number density of nitrogen bubbles [*Mourtada-Bonnefoi*, 1998; *Gardner et al.*, 1999] and are not appropriate to study bubble nucleation. The second requirement is that the starting glasses be crystal-free because heterogeneous nucleation of bubbles on crystals is much easier than homogeneous nucleation in the liquid [*Hurwitz and Navon*, 1994]. In a decompression experiment the presence of crystals may therefore lead to an early

Table 1. Composition of Güney Dagi Obsidian (GDO)[a]

Oxides	GDO 1	GDO 2	FGDO
SiO_2	76.51	76.56	
Al_2O_3	12.56	13.39	
Fe_2O_3	0.78	0.80	
MgO	0.01	0.08	
CaO	0.25	0.39	
Na_2O	4.47	4.22	
K_2O	4.24	4.44	
TiO_2	0.03	0.04	
MnO	0.07	0.07	
H_2O	1.39[b]		1.43[c]
CO_2[d]	200 (20) ppm		362[c]
Cl[d]	634 (38) ppm		
F[d]	710 (21) ppm		
S[d]	<100 ppm		

[a] GDO composition 1 is by ICP analysis, Clermont-Ferrand, and GDO composition 2 is from *Druitt et al.* [1995]. The oxides are given in wt % with errors comprised between 0.5 and 2% relative; all Fe is reported as Fe_2O_3. The glass FGDO was produced by fusing GDO obsidian at 1200°C and 1 GPa in a piston-cylinder apparatus for 64 min.

[b] H_2O concentration estimated by a loss on ignition at 1000°C (including 0.06 wt % loss at 120°C).

[c] The H_2O and CO_2 concentrations in FGDO were measured by FTIR spectrometry (the error is 0.02 wt % for H_2O and 5 ppm for CO_2).

[d] CO_2 (coulometry), Cl (colorimetry), F (potentiometry), and S (coulometry) in composition 1 were analyzed at the Centre de Recherches Pétrographiques et Géochimiques (Nancy); S was below the detection limit (100 ppm); the errors are given in parentheses.

event of heterogeneous nucleation that will in turn reduce the water content in the liquid and affect the subsequent homogeneous nucleation behavior.

2.1.1. Preparation of starting glasses. [4] Bubble-free and crystal-free hydrous rhyolitic glasses were prepared by hydrating obsidian cylinders at 1000°C. A calc-alkaline, rhyolitic obsidian from Güney Dagi, Turkey, was used as the starting composition in our study (Table 1) [*Druitt et al.*, 1995]. Güney Dagi obsidian (GDO) consists of a dark glass containing <1 vol % microlites of K-feldspar, plagioclase, amphibole, ilmenite, magnetite, epidote, and zircon. The volatile content of GDO is 1.4 wt % H_2O and 200 ± 20 ppm CO_2 (Table 1). For comparison, the glass FGDO produced by fusing GDO at 1200°C and 1 GPa in a platinum container in a piston-cylinder apparatus for 64 min contained 1.43 ± 0.02 wt % H_2O and 362 ± 5 ppm CO_2 (Table 1). The larger CO_2 content of FGDO compared to GDO is due to contamination by the graphite furnace of the piston-cylinder assembly as discussed in section 2.1.2. The large H_2O and CO_2 contents in GDO suggest the presence of hydrated and carbonated phases among the microlites because the glass phase of the obsidian contains only 1.05 ± 0.05 wt % H_2O and no CO_2 (<1 ppm).

[5] Cylinders 2.5 mm in diameter were cored from a large block of Güney Dagi obsidian and were used to prepare six types of starting glasses with different volatile contents: H5 (4.1–4.5 wt % H_2O, 50 ppm CO_2), H8 (7.7 wt % H_2O, 10 ppm CO_2), H5C/Ni (4.5–4.9 wt % H_2O, 800 ppm CO_2), H5C/Cu (4.4–4.7 wt % H_2O, 1150 ppm CO_2), H7C/Ni (6.7–7.2 wt % H_2O, 500 ppm CO_2), and H7C/Cu (6.6–7.0 wt % H_2O, 400 ppm CO_2). These volatile compositions cover most of the range of H_2O and CO_2 contents of rhyolitic magmas [*Johnson et al.*, 1994]. The CO_2-poor glasses were prepared in water saturation experiments by equilibrating the obsidian GDO with an H_2O-rich fluid, in an internally heated pressure vessel at 150 MPa (H5) or 280 MPa (H8). A 12 mm long cylinder of GDO was loaded along with distilled water into a gold capsule (wall thickness of 0.2 mm); the amount of added water was larger than the amount required to saturate the obsidian at the pressure-temperature (*P-T*) conditions of the saturation experiment. The capsule was cooled with liquid nitrogen during arc welding to avoid water vaporization. The saturation experiments were performed at 1000°C for 3–4 days (Table 2); in three experiments the temperature was reduced to 850°C (H5-8 and H5-9) or 800°C (H5-11) for 2 days prior to quench. After the saturation experiment, the glass cylinder was cut into short pieces, 2–3 mm long, that were cleaned in distilled water before being used in a nucleation experiment.

[6] The CO_2-rich glasses, H5C/Ni, H5C/Cu, H7C/Ni, and H7C/Cu, were prepared in a piston-cylinder apparatus at 1 GPa and 1000°C (Table 3). A cylinder of obsidian, 1.9–3.3 mm long, was fitted into a platinum capsule (wall thickness of 0.2 mm) along with a precise quantity of distilled water; by immersing the bottom half of the capsule into water it was possible to minimize water loss during arc welding to a negligible level. Given the natural water content of GDO (1.4 wt %; Table 1), quantities of 3.1 and 5.5 wt % of distilled water were added to end with total contents of ≈4.5 and 6.9 wt % H_2O, respectively, after hydration. We used an encapsulation technique similar to the technique developed by *Ayers et al.* [1992]: the platinum capsule was placed in an external, thick-walled container made of either nickel (for glasses H5C/Ni and H7C/Ni) or copper (for glasses H5C/Cu and H7C/Cu). The external container was then filled with 100 μL of distilled water and ≈100 mg of buffer (Ni-NiO or Cu-Cu_2O). These buffers correspond to oxygen fugacities in the range of natural conditions [*O'Neil and Pownceby*, 1993; *Johnson et al.*, 1994]. The Ni or Cu container was covered with a lid of the same metal and placed in a NaCl-pyrex-graphite-crushable MgO assembly. The duration of the hydration experiments ranged from 1–2.5 days for glasses H7C/Ni and H7C/Cu to 2.9–4 days for glasses H5C/Ni and H5C/Cu (Table 3).

2.1.2. Volatile contents of starting glasses. [7] The techniques used to determine the volatile content of starting glasses are Fourier transformed infrared (FTIR) spectrometry (see section 2.3 for technical information) and mass balance calculations (for H_2O only; see Table 2, footnote b, and Table 3, footnote b). FTIR spectrometry is the most accurate technique, but it could not be applied systematically on starting glasses because it is a destructive method (the glass plates prepared for FTIR spectrometry are too thin to be used in decompression experiments). Accordingly, direct measurements of volatile contents by FTIR spectrometry were only made on six starting glasses. In addition, H_2O and CO_2 concentrations were measured by FTIR spectrometry on six glassy samples from decompression

Table 2. Synthesis Conditions of Glasses H5 and H8

Run[a]	*P*, MPa	*T*, °C	t_h, days	H_2O[b]	H_2O[c]	CO_2[c]
H5-3[d]	150	1000	3.7	4.5		
H5-4[d]	150	1000	3.7	4.0		
H5-5	150	1000	3	4.2		
H5-6	150	1000	3	4.2	4.09	49
H5-8[e]	150	1000/850	4/2	4.7		
H5-9[e]	150	1000/850	4/2	4.3		
H5-11[e]	150	1000/800	4/2	4.8		
H8-17	280	1000	4	7.7	7.66	10

[a] The number hyphenated after glass type H5 or H8 is the number of the water saturation experiment.

[b] Water content of the rhyolitic glass (in wt %) is calculated by mass balance. At the end of each saturation experiment, the mass of excess water not dissolved into the obsidian was measured by piercing the gold capsule and measuring the weight loss at 110°C. From the total amount of water loaded in the capsule and the initial water content in GDO, it was then possible to compute the water content of the saturated rhyolitic glass.

[c] H_2O (wt %) and CO_2 (ppm) were measured by FTIR spectrometry.

[d] Here the GDO cylinder is 20 mm long. The GDO cylinder used in all other saturation experiments was only 12 mm long.

[e] Two-step experiments with a 4 day step at 1000°C followed by a 2 day step at 850°C (H5-8 and H5-9) or 800°C (H5-11).

Table 3. Synthesis Conditions of Glasses H5C/Ni, H5C/Cu, H7C/Ni, and H7C/Cu[a]

Run	t_h, hours	H_2O[b]	CO_2[c]
	H5C/Ni		
14	86.77	4.6	(829)
15	84.10	4.5	(809)
28[d]	92.33	4.6 [4.75]	802
31	75.58	4.6	(746)
32	70.27	4.6 [4.92]	801
	H5C/Cu		
19	66.33	4.5	
20[d]	66.25	4.5 [4.39]	1222
29	89.33	4.6	
33	69.82	4.5 [4.44]	1077
39	69.03	4.7	
	H7C/Ni		
3	27.00	6.9	(388)
4[d]	26.83	6.9 [7.04]	360
5	26.33	7.0	(383)
9	29.63	6.9	(407)
10	43.22	6.7	(508)
11	48.00	6.8	(543)
12	60.00	7.0	(631)
13	60.00	6.9	(631)
35	38.10	7.2	(470)
36	46.33	7.0	(531)
37	45.30	6.8	(523)
38	45.85	6.8	(527)
41	44.30	6.8 [6.87]	559
	H7C/Cu		
23	23.50	6.9	(362)
24	27.42	6.8	(391)
25	23.50	6.9	(362)
30	39.42	7.0	(480)
40	31.00	6.6	(417)
43	28.08	6.9 [6.95]	342

[a] Glasses H5C/Ni, H5C/Cu, H7C/Ni and H7C/Cu were hydrated in a piston-cylinder apparatus at 1 GPa and 1000°C (run durations are listed in the t_h column).

[b] Water contents (in wt %) were computed from the mass of distilled water loaded in the platinum capsule along with the GDO cylinder. Water contents directly measured by FTIR spectrometry are given in brackets.

[c] CO_2 contents (ppm) were measured by FTIR spectrometry. The numbers in parentheses correspond to the CO_2 contents computed from run durations t_h (see text for further explanation).

[d] For glass numbers 4, 20, and 28 the measurements of H_2O and CO_2 contents by FTIR spectroscopy were made after the decompression experiment.

experiments in which no homogeneous nucleation occurred. The volatile content in the core of these six samples is supposed to be equal to the volatile content of the starting glass: in the absence of vesiculation the volatile content in the core can only be lowered by volatile diffusion from the core to the rim of the glass cylinder; the duration of the decompression experiments is, however, too short for diffusion to have a measurable effect over a length scale longer than a few hundreds of micrometers. At the end of most decompression experiments, the core of the sample was crowded with bubbles so that FTIR spectrometry was not applicable.

2.1.2.1. Volatile content in the CO_2-poor glasses: [8] FTIR spectrometry yielded a water content of 4.09 wt % in glass H5-6 and 7.66 wt % in glass H8 (Table 2). These values are in perfect agreement with the H_2O contents calculated by mass balance from the amount of water dissolved into the obsidian during the saturation experiments: 4.2 wt % in glass H5-6 and 7.7 wt % in glass H8. By comparison, the solubility of water in rhyolitic liquids lies in the range 4.0–5.0 wt % water at 150 MPa and 6.5–8.3 wt % at 280 MPa [*Silver et al.*, 1990; *Wallace et al.*, 1995; *Gardner et al.*, 1999; *Tamic et al.*, 2001]. Because starting glasses H5-3 to H5-5 were water saturated at the same conditions as glass H5-6 (150 MPa and 1000°C), their water content is assumed to be equal to ≈4.1 wt %. Water contents calculated by mass balance in glasses H5-3 to H5-5 range from 4.0 to 4.5 wt %.

[9] We do not have a direct measurement by FTIR spectrometry of the water content of glasses H5-8, H5-9, and H5-11 water saturated at 150 MPa and 800–850°C. We anticipate, however, that their water content is only slightly larger (by ≈0.4 wt %) than in glass H5-6 water saturated at 150 MPa and 1000°C for the following reasons: (1) *Holtz et al.* [1992] showed that the water solubility in an haplogranitic melt at 2 kbar only increased by ~0.4 wt % when the temperature decreased from 1000° to 800°C; (2) water contents calculated by mass balance are just slightly larger in glasses H5-8, H5-9, and H5-11 (4.3–4.8 wt %; Table 2) than in glasses H5-3 to H5-6 (4.0–4.5 wt %).

[10] CO_2 concentration is equal to ≈50 ppm in glass H5-6 and to 10 ppm in glass H8 (Table 2). In addition, CO_2 contents of 31, 108, and 71 ppm were measured after three decompression experiments in which H5 was used as starting glass (runs VGD20, VGD17, and VGD24, respectively). The lower CO_2 contents in glasses H5 and H8 compared to the CO_2 concentration in GDO (200 ppm; Table 1) are due to the preferential partitioning of CO_2 into the aqueous fluid phase coexisting with the rhyolitic liquid during the water saturation experiments.

2.1.2.2. Volatile content in the CO_2-rich glasses: [11] H_2O concentrations range from 4.4 to 4.9 wt % in glasses H5C/Ni and H5C/Cu and from 6.6 to 7.2 wt % in glasses H7C/Ni and H7C/Cu (Table 3). There is a very good agreement between the water contents calculated by mass balance and the water contents measured by FTIR spectrometry in seven starting glasses: the difference between the two values is equal to 0.3 wt % in one sample, but in the six other samples it is smaller than 0.2 wt %.

[12] The CO_2 contents of the glasses prepared in a piston-cylinder apparatus are higher than the initial CO_2 concentration in GDO and increase markedly with the duration of the hydration experiment (Figure 1 and Table 3). The CO_2 enrichment relative to GDO is due to sample contamination by carbon coming from the graphite furnace of the piston-cylinder assembly [*Brooker et al.*,

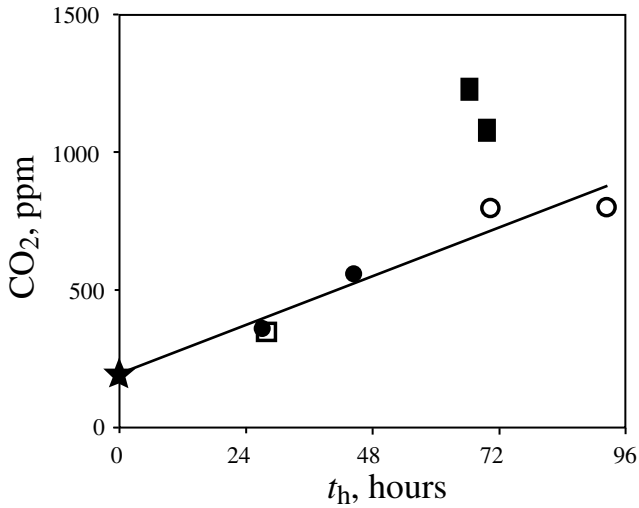

Figure 1. Concentrations of CO_2 in glasses H5C/Ni (open circles), H5C/Cu (solid squares), H7C/Ni (solid circles), and H7C/Cu (open square) as a function of the duration t_h of the hydration experiment. The CO_2 concentration in obsidian GDO is shown by the star. The line is the best linear fit to CO_2 concentrations in GDO and in glasses H5C/Ni, H7C/Ni, and H7C/Cu ($CO_2 = 7.38t_h + 188.61$).

Table 4a. Decompression Experiments Using Glasses H5 and H8[a]

Sample	Glass[b]	P_i, MPa	t_D,[c] s	P_f, MPa	t, s	V_{bulk},[d] %	Texture[e]
VGD17[f]	H5-6	200	n.d.	n.d.	n.d.	n.d.	NB
VGD18[f]	H5-5	200	n.d.	n.d.	n.d.	n.d.	NB
VGD5[g]	H5-4	200	0.3(533)	40.1	60	9.6	BFC
VGD6[g]	H5-4	200	0.3(533)	40.0	3600	19.3	BFC
VGD8[g]	H5-3	200	0.3(533)	40.0	39600	38.9	BFC
VGD19[h]	H5-5	200	3.7(43.9)	37.7	64	n.d.	BFC
VGD23	H5-8	200	2.0(81.1)	37.9	62	14.7	BFC
VGD22	H5-8	200	29(5.5)	39.2	3600	41.0	BFC
VGD24	H5-8	200	1.5(108)	38.0	60	7.9	BFC
VGD48	H5-11	200	52(3.1)	41.0	120	19.6	BFC
VGD49	H5-11	200	43(4.2)	20.9	120	27.5	BFC
VGD10	H5-3	200	2.3(77.4)	22.0	300	24.2	BFC
VGD13	H5-4	200	202(0.9)	10.2	300	27.1	BFC
VGD27	H5-9	200	42(4.5)	10.2	1800	n.d.	Pum
VGD28	H5-11	200	88(2.2)	5.7	60	n.d.	Pum
VGD26	H5-9	200	20(9.7)	5.1	12	n.d.	Pum
VGD25	H5-9	200	18(10.8)	5.1	180	n.d.	Pum
VGD15	H5-6	200	127(1.5)	4.0	60	66.4	BFC
VGD16	H5-6	200	91(2.2)	4.0	12	64.3	BFC
VGD20	H5-5	200	43(4.5)	4.9	10	28.6	BFC
VGD14	H5-6	200	138(1.4)	4.2	300	76.6	Pum
VGD21	H5-5	200	62(3.2)	0.1	13	30.3	BFC
VGD12	H5-3	200	103(1.94)	0.1	300	n.d.	Pum
VGD67	H8-17	295	72(1.0)	220	119	n.d.	BFC
VGD66	H8-17	295	116(1.0)	179	120	n.d.	HoN
VGD65	H8-17	295	160(1.0)	140	120	n.d.	HoN
VGD64	H8-17	295	220(1.0)	79	121	n.d.	HoN

[a] Decompression experiments were run at 800°C and comprised a first step of 15 min at pressure P_i, a decompression step of duration t_D, and a nucleation step of duration t at a pressure P_f.
[b] Details about the water saturation runs can be found in Table 2.
[c] The number in parentheses is the "linear" decompression rate $(P_i - P_f)/t_D$ (in MPa s^{-1}).
[d] Bulk vesicularity (vol %) of the sample at the end of the experiment; n.d. is not determined.
[e] Final texture is labeled as follows: NB, no bubble; BFC, bubble-free core; HoN, homogeneous nucleation texture; Pum, entirely vesiculated pumice.
[f] Samples VGD17 and VGD18 were quenched directly after 30 and 90 min, respectively, at 200 MPa at 800°C.
[g] The pressure was decreased "instantaneously" by opening a valve connecting the pressure vessel at 200 MPa to a pressure line of fixed volume at atmospheric pressure: this procedure yielded a very large decompression rate and a reproducible final pressure.
[h] Experiment was run with a gold capsule instead of a platinum one.

1998]. For glasses H5C/Ni, H7C/Ni, and H7C/Cu the CO_2 enrichment is well described by the linear relationship: $CO_2 = 7.38t_h + 188.61$, where CO_2 is in parts per million and the duration t_h of the hydration experiments is in hours (Figure 1). Glasses H5C/Cu have much larger CO_2 contents (1070–1220 ppm) than glasses H5C/Ni (800 ppm) despite similar run durations (~3 days). Platinum capsules retrieved from copper external containers after 3–4 days at 1000°C and 1 GPa were strongly recrystallized and showed a pinkish color. Recrystallization presumably resulted in an increased effective permeability of the platinum capsule to carbon and could explain the stronger CO_2 enrichment in glasses H5C/Cu. For glasses H5C/Ni, H7C/Ni, and H7C/Cu, in which CO_2 concentration was not directly measured by FTIR spectrometry, a first-order estimate was obtained from the run duration by using the relationship $CO_2 = 7.38t_h + 188.61$ (Table 3). The mean calculated CO_2 concentration increases from 400 ppm in H7C/Cu to 500 ppm in H7C/Ni to 800 ppm in H5C/Ni.

2.2. Decompression Experiments

[13] We performed 49 isothermal decompression experiments to produce homogeneous bubble nucleation in volatile-rich rhyolitic liquids containing 4.1–7.7 wt % H_2O and up to 1200 ppm CO_2 (run details are summarized in Tables 4a and 4b). The decompression experiments were performed in an externally heated pressure vessel made of a nickel-based superalloy (Nimonic 105) and fitted with a rapid-quench extension [*Ihinger*, 1991; Ihinger, written communication, 1995]. The sample was a short cylinder (diameter of 2.5 mm and length of 2–3 mm) of bubble- and crystal-free rhyolitic glass, prepared as described in section 2.1 and welded in a platinum container. It was first pressurized using nitrogen gas to a pressure P_i and then heated to 800°C in ~60–90 min. P_i equaled 200, 285, and 295 MPa for water contents of 4–5, ≈7.0, and 7.7 wt %, respectively. Pressure was measured by a pressure transducer precisely to <1 MPa. Pressure was maintained to ±5MPa at P_i during the heating stage. After 15 min at 800°C and pressure P_i, the pressure was decreased to a value P_f lower than the saturation pressure P_{Sat} via a controlled leak in the pressure line. The decompression duration ranged from a few seconds to a few minutes, leading to quasi-linear decompression rates of typically 1–10 MPa s^{-1} (larger rates, sometimes in excess of 100 MPa s^{-1}, were used in the first decompression experiments; see Table 4a). The final step at 800°C and pressure P_f typically lasted 2 min and is thereafter referred to as the nucleation step. The durations t_D of the decompression step and t of the nucleation step were precisely measured by registering the pressure as a function of time on a strip chart recorder. The nucleation experiments were terminated by an isobaric quench at an initial rate of 200°C s^{-1}.

2.3. Analytical Techniques

2.3.1. Volatile contents. [14] The volatile content of representative glasses was measured by FTIR spectrometry and microprobe analysis. FTIR spectrometry was made at the University of Bristol using a Nicolet 800 spectrometer operating from 8000 to 400 cm^{-1} with a KBr beamsplitter, a MCT detector, and a resolution of 4 cm^{-1}, the signal being averaged over 256 scans. Doubly polished sections of the samples were placed under a microscope coupled to the spectrometer and enclosed in a box

Table 4b. Decompression Experiments Using Glasses H5C/Ni, H5C/Cu, H7C/Ni, and H7C/Cu

Sample	Glass[a]	P_i, MPa	t_D,[b] s	P_f, MPa	t, s	Texture[c]
VGD50	H5C/Ni-28	200	19 (5.2)	101	120	BFC
VGD42	H5C/Ni-15	200	19 (7.2)	63	121	HoN
VGD41	H5C/Ni-14	200	43 (3.7)	41	115	HoN
VGD53	H5C/Ni-31	200	30 (5.6)	32	120	HoN
VGD46	H5C/Cu-19	200	52 (1.3)	131	120	BFC
VGD47	H5C/Cu-20	200	43 (2.2)	104	120	BFC
VGD58	H5C/Cu-33	202	50 (2.8)	61	122	BFC
VGD62	H5C/Cu-39	200	63.5 (2.7)	29	120	HoN[d]
VGD32[e]	H7C/Ni-4	285	n.d.	n.d.	n.d.	BFC
VGD39	H7C/Ni-12	285	43 (1.7)	211	121	HoN[d]
VGD38	H7C/Ni-11	285	20 (4.3)	198	120	HoN
VGD57	H7C/Ni-35	285	33 (3.1)	183	120	HoN
VGD37	H7C/Ni-10	285	17 (7.9)	150	120	HoN
VGD61	H7C/Ni-37	287	21 (6.6)	148	1	HoN
VGD33	H7C/Ni-5	285	27 (5.3)	141	121	HoN
VGD59	H7C/Ni-38	287	27.5 (6.8)	100	121	HoN
VGD60	H7C/Ni-36	287	29 (6.5)	99	2.5	HoN
VGD31	H7C/Ni-3	285	27 (8.7)	51	122	HoN
VGD36	H7C/Ni-9	285	10 (23.5)	50	5400	HoN
VGD69[e]	H7C/Cu-43	285	n.d.	n.d.	n.d.	BFC
VGD52	H7C/Cu-30	285	10 (3.9)	246	120	HoN
VGD45	H7C/Cu-25	285	15 (3.7)	229	124	HoN
VGD44	H7C/Cu-24	285	15 (5.5)	202	121	HoN
VGD43	H7C/Cu-23	285	13 (9.9)	157	120	HoN
VGD63	H7C/Cu-40	286	37 (5.6)	80	120	HoN

[a] The number after the hyphen is the number of the hydration run (Table 3).
[b] The number in parentheses is the "linear" decompression rate $(P_i - P_f)/t_D$ (in MPa s^{-1}).
[c] Texture of the sample at the end of the nucleation experiment, as in Table 4a.
[d] Special type of HoN texture in which a very small number of large bubbles (~30 in VGD39, 16 in VGD62; see Figure 7) was observed in the core of the sample.
[e] Samples VGD32 and VGD69 were quenched directly after 15 min at 285 MPa and 800°C.

continuously purged with high-purity nitrogen to reduce atmospheric H_2O and CO_2 to a very low level. Using the Beer-Lambert law, molecular H_2O, OH^-, and molecular CO_2 contents were derived from the height of the absorbance peaks at 5200, 4500, and 2350 cm^{-1} wave numbers, respectively, using molar absorptivities of 1.61, 1.73, and 1077 L mol^{-1} cm^{-1}, respectively [*Newman et al.*, 1986; *Blank*, 1993]. The density of the glasses was computed following the method of *Lange and Carmichael* [1987], from GDO oxide composition (Table 1), at a temperature of 1000°C and with a correction for the water content given the molar volume of water in rhyolitic glasses of 12.0 cm^3 mol^{-1} [*Silver et al.*, 1990]. The resulting densities equal 2300, 2260, 2230, and 2223 kg m^{-3} for water contents of 1.4, 4.5, 7.0, and 7.7 wt %, respectively. After recording the spectra, the thickness of the doubly polished sections was measured using a digital travel gauge with an accuracy of ±1 μm. The variation of the thickness was used to estimate the uncertainty on the final volatile content.

[15] In some samples that conserved bubble-free cores after the nucleation experiment the glass composition was analyzed with a Cameca Sx 100 electron microprobe. The analytical conditions were 15 kV, 5 nA, a counting time of 10 s, and a defocused beam 16 μm in diameter; the following elements were analyzed: SiO_2, Al_2O_3, FeO, MgO, CaO, Na_2O, K_2O, TiO_2, and MnO. The volatile content was derived by the difference method [e.g., *Martel et al.*, 1998], assuming that the total volatile content is equal to 100% minus the total of the major elements. Because of its poor accuracy the difference method was merely used to look for gradients in H_2O concentrations.

2.3.2. Textural parameters. [16] At the end of a decompression experiment, the sample was fractured in two halves. One half was coated with carbon and gold for direct observation of the fracture surface by scanning electron microscopy (SEM). The other half was mounted in epoxy, polished, and carbon-coated for SEM imaging. The SEM microphotographs of the core of the samples were then analyzed with the National Institute of Health (NIH) Image software to quantify bubble size distribution, mean bubble size d, bubble number density per unit volume of liquid N, and vesicularity V. Three-dimensional (3-D) bubble size distributions were derived from 2-D image analysis using the reformulation of Johnson-Saltykov's method [*Saltykov*, 1967; *Coster and Chermant*, 1989].

3. Experimental Results

3.1. Main Textural Types

[17] We distinguished two main types of samples as a function of their internal textures: the samples with a bubble-free core and those with a bubbly core usually characterized by a large number density of uniformly spaced bubbles.

3.1.1. Bubble-free cores. [18] The fracture surface of many samples showed a large, glassy core completely devoid of bubbles and a thin bubbly rim (Figure 2a). Most bubbles were in direct contact with the platinum capsule and formed by heterogeneous nucleation on the inner wall of the container. Some bubbles were, however, completely embedded in the rhyolitic glass and could not result from heterogeneous nucleation on platinum. In most cases, these bubbles were concentrated along planar arrays or slightly curved surfaces (Figure 2a). Presumably, these structures were related to fractures in the border of the starting glass where some air got trapped. At high temperature the fracture healed, leaving an array of small nitrogen-rich bubbles; during the decompression and nucleation steps of the experiment, these bubbles grew by diffusion of water to yield almost continuous arrays of large bubbles (or "bubbly fractures"). The bubble-free cores are clearly indicative of the absence of any nucleation event neither homogeneous nor heterogeneous in the center of the

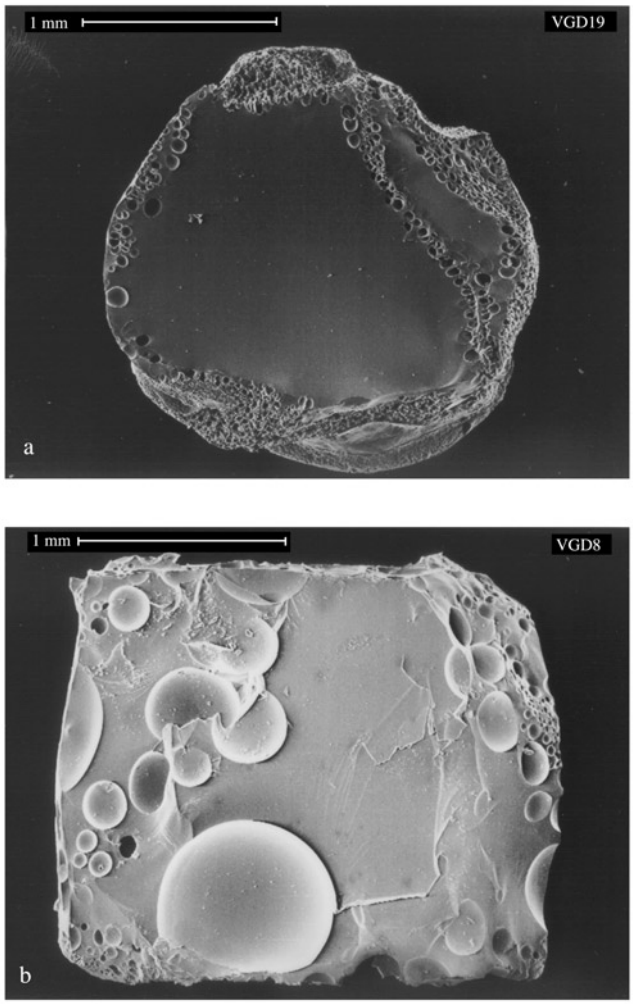

Figure 2. Scanning electron micrographs of fracture surfaces of samples VGD19 and VGD8 (glass type H5). (a) Micrograph of sample VGD19 (P_f = 37.7 MPa, t = 64 s) showing a bubble-free core, a bubbly rim, and a "bubbly fracture." (b) Micrograph of sample VGD8 (P_f = 40 MPa, t = 11 hours) showing a shrinking bubble-free core and giant bubbles growing inward (the cluster of bubbles on the left is presumably a bubbly fracture).

sample. We checked that the absence of bubbles was not due to water loss: microprobe profiles in samples with a bubble-free core show a pattern characterized by a plateau of large water content in the core and lower contents in the rim (Figure 3). The lower H_2O contents in the rim result from the diffusion of water into bubbles growing on or close to the platinum inner wall. The thickness of the water-depleted rim increases with increasing duration of the nucleation step but remains relatively small: for example, 200 μm for glass type H5 at t = 3600 s (VGD6 in Figure 3).

3.1.2. Homogeneous nucleation textures. [19] At the end of the nucleation experiment, many samples displayed a core with a large number density of uniformly spaced bubbles (Figure 4). Because these samples did not contain crystals or visible impurities that could serve as sites for heterogeneous bubble nucleation and because of the homogeneity of the texture, the core bubbles can be ascribed to an event of homogeneous bubble nucleation. The samples with a homogeneously nucleated core always showed a very distinct rim, <400 μm wide. At high values of the pressure P_f this rim was bubble-free except at the contact with the capsule (Figure 4a). At lower values of P_f the rim only differed from the core by a lower bubble number density and a larger mean bubble size (Figure 4b).

3.2. Nucleation Behavior of Compositions H7C/Ni and H7C/Cu

[20] We first describe the nucleation behavior in the two best documented series: H7C/Ni and H7C/Cu. The trends obtained by these two series also give the qualitative trends followed by the other compositional series. Owing to their large CO_2 content, glasses H7C/Ni and H7C/Cu have volatile saturation pressures larger than 300 MPa (see section 4). For safety reasons we could not work above 300 MPa in our externally heated pressure vessel (at 800°C). Accordingly, the first step of the nucleation experiments with glasses H7C was made at a pressure P_i = 285 MPa, slightly lower than the volatile saturation pressure. The pressure P_i was, however, significantly larger than the critical nucleation pressure of compositions H7C/Ni and H7C/Cu (see below; the critical pressure of nucleation P_{HoN} is defined as the maximum pressure at which homogeneous bubble nucleation can occur in a given composition). Consequently, the fact that P_i was lower than P_{Sat} in series H7C/Ni and H7C/Cu had no effect on the nucleation behavior of the sample cores, as confirmed by the following observations: (1) The bubble-free cores in samples VGD32 and VGD69 that were directly quenched at the end of the 285 MPa step demonstrate that no homogeneous bubble nucleation occurred before decompression in composition H7C/Ni and H7C/Cu. (2) Some bubble nucleation occurred at the contact of the platinum container before decompression because $P_i > P_{Sat}$. However, the duration of the step at P_i was very short (15 min), so that volatile diffusion toward the marginal bubbles only affected the rim of the rhyolite cylinder over a distance of a few hundreds of micrometers: the volatile content in the core remained unchanged. For instance, the water concentrations measured by FTIR spectrometry in the core of the glasses at the end of decompression experiments VGD32, VGD47, and VGD50 are equal to the water contents of the starting glasses measured by mass balance (Table 3). Volatile depletion in the outer few hundreds of micrometers of the samples is responsible for the development of a distinct rim, either glassy or bubble-poor, below P_{HoN} (Figure 4).

3.2.1. Nucleation behavior in composition H7C/Ni. [21] For all the experiments at $P_f \leq$ 198 MPa, glasses H7C/Ni yielded a very typical homogeneous nucleation texture with a core crowded with more or less uniformly spaced bubbles (Figures 4 and 5). In the nucleation experiment at P_f = 211 MPa (VGD39, Table 4b) the sample was almost bubble-free except near its center where ~20 large bubbles were observed. The very low bubble number density in VGD39 ($\approx 10^{11}$ m^{-3}) is presumed to mean that the experiment was run at a pressure P_f just slightly below the critical nucleation pressure P_{HoN} for volatile composition H7C/Ni. P_{HoN} is defined as the maximum pressure at which homogeneous bubble nucleation can occur. A major experimental result is the strong dependence of nucleation texture on pressure P_f for duration t fixed at 2 min (Figures 5a–5d and Table 5). At large values of P_f the evolution with decreasing P_f goes from a nucleation texture with a moderate number density of medium-sized bubbles (in VGD38, Figure 5a) to a texture with a very large number density of small bubbles (in VGD33, Figure 5c). Below ~140 MPa the trends are reversed: the bubble number density decreases slightly, and the mean bubble size increases with decreasing P_f (Figures 5d and 6).

3.2.2. Nucleation behavior in composition H7C/Cu. [22] Five experiments were performed using glasses H7C/Cu at P_f ranging from 259 to 80 MPa. They all resulted in extensive homogeneous bubble nucleation. The evolution of bubble number density and mean bubble size with decreasing P_f are similar to those described for composition H7C/Ni but are slightly shifted toward higher values of P_f (Figure 6 and Table 5).

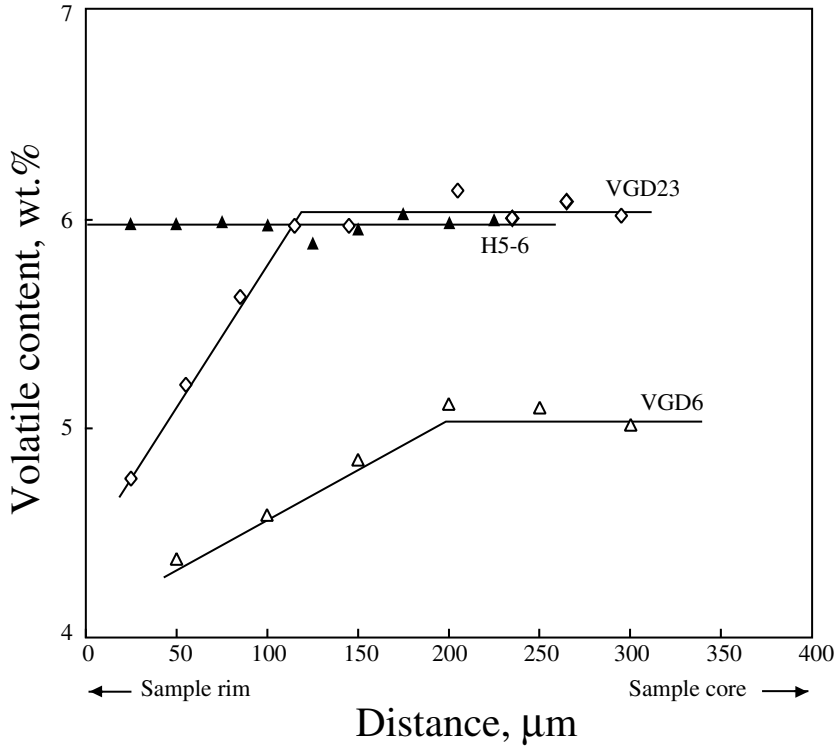

Figure 3. Volatile concentration profiles in samples VGD6 (P_f = 40 MPa, t = 1 hour) and VGD23 (P_f = 37.9 MPa, t = 62 s) and in starting glass H5-6 (Table 2). The volatile content was computed from electron microprobe analyses using the difference method (this method may significantly overestimate the volatile content and is merely used to visualize gradients in water concentrations).

3.2.3. Timing of nucleation: Competition between nucleation and coalescence. [23] Two experiments with $t \approx 0$ (VGD61 and VGD60) were made in the H7C/Ni series to constrain the timing of homogeneous bubble nucleation (Table 4b). These two experiments can be directly compared with two other experiments (VGD37 and VGD59) with similar decompression rates of 6.5–7.9 MPa s^{-1}, which were performed at the same pressure P_f but a higher t of 2 min. After decompression to 148 MPa, the number density of bubbles N increased with t from 2.5 $\times$ 10^{14} m^{-3} for t = 1 s (VGD61) to 3.4 $\times$ 10^{14} m^{-3} for t = 120 s (VGD37), implying that a large proportion of bubbles nucleated during the decompression step. In contrast, after decompression to 100 MPa, the relationship between VGD59 and VGD60 is reversed: the bubble number density decreases by half between 2.5 s and 2 min. The explanation to this paradox seems to be coalescence as sample VGD60 is characterized by a large number of quenched coalescence figures (Figures 5f and 5g), whereas such features are almost absent in VGD59 (Figure 5e). Also, the mean bubble size increases from 8.6 μm in VGD60 to 9.8 μm in VGD59, in good agreement with a process of coalescence.

[24] The importance of coalescence is also well illustrated in the evolution from VGD31 (P_f = 51 MPa, t = 122 s, Figure 5d) to VGD36 (P_f = 50 MPa, t = 90 min, Figure 5h). These two samples have similar vesicularities, but VGD36 has a much lower N and larger d than VGD31. The numerous quenched coalescence figures in VGD31 (Figure 5d) suggest that bubble coalescence is the main process involved in the reduction of N with increasing t.

3.3. Nucleation Behavior of Composition H5C/Ni and H5C/Cu

[25] Four experiments were performed using glasses H5C/Ni at P_f = 101, 63, 41, and 32 MPa. The experiment at P_f = 101 MPa yielded a bubble-free core, whereas the experiments at $P_f \leq 63$ MPa had a densely nucleated core (Table 4b). At P_f = 101, 63, and 41 MPa the sample rim was bubble-free; at P_f = 32 MPa it contained a low number density of large bubbles. The behavior of glasses H5C/Cu is documented by four experiments. A bubble-free core was obtained in nucleation experiments at P_f = 131, 104, and 61 MPa. In the nucleation experiment at P_f = 29 MPa (VGD62, Table 4b), the sample was almost bubble-free except near its center, where 16 large bubbles (102 μm mean diameter) were observed (Figure 7). The very low bubble number density in VGD62 (5 $\times$ 10^{10} m^{-3}) suggests that the experiment was run at a pressure P_f just slightly below the critical nucleation pressure for volatile composition H5C/Cu.

3.4. Nucleation Behavior of Composition H8

[26] Four nucleation experiments were performed using the rhyolitic glass water saturated at 280 MPa. They were made at P_f = 220, 179, 140, and 79 MPa with a decompression rate of 1.0 MPa s^{-1} (VGD67-64 in Table 4a). The experiment at 220 MPa produced a bubble-free core texture. Homogeneous bubble nucleation was observed in the three other experiments at $P_f \leq$ 179 MPa (Figure 8a). The bubble number density increased from 3.8 $\times$ 10^{12} m^{-3} at P_f = 179 MPa to 1.2 $\times$ 10^{13} m^{-3} at P_f = 140 MPa to 3.9 $\times$ 10^{13} m^{-3} at P_f = 79 MPa. These values are markedly lower than those measured in the H7C series. The mean bubble size is large and only slightly sensitive to P_f (Figure 8b and Table 5).

3.5. Nucleation Behavior of Composition H5

[27] Twenty-one decompression experiments were performed using glasses H5 as starting materials (Table 4a). Two experiments, VGD17 and VGD18, were also run to check that the rhyolitic

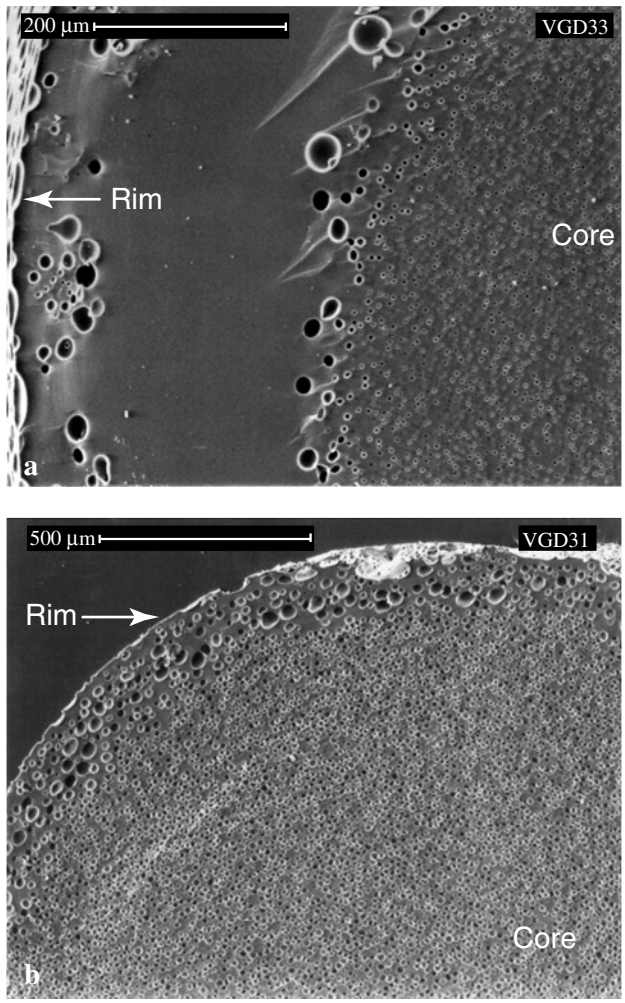

Figure 4. Scanning electron micrographs of fracture surfaces of samples VGD33 and VGD31 (glass type H7C/Ni). (a) Micrograph of sample VGD33 (P_f = 141 MPa, t = 121 s) showing a thin layer of bubbles nucleated at or close to the contact with the platinum container, a 250 μm wide glassy zone, and a layer of larger bubbles separating the glassy rim from the core. The core is characterized by a large number density of small bubbles. (b) Micrograph of sample VGD31 (P_f = 51 MPa, t = 122 s) showing extensive bubble nucleation both in the core and in the rim. The rim has a lower bubble number density and a larger mean bubble size than the core.

liquids did not nucleate bubbles at 200 MPa and 800°C, that is, before the decompression step of the nucleation experiment. The main experimental results were reported by *Mourtada-Bonnefoi and Laporte* [1999] and may be summarized as follows.

1. At values of $P_f \geq 10$ MPa, all samples had a bubble-free core at the end of the nucleation experiment (e.g., VGD19 in Figure 2a). At small values of t, a few minutes or even 1 hour, the bubbly rim was very narrow, and the bubbles rarely exceeded 100 μm in diameter. The textural evolution with increasing run duration was studied at $P_f \approx 40$ MPa: even after a nucleation step of 11 hours, no homogeneous bubble nucleation occurred in the inner core of the sample, and the evolution was dominated by the diffusive growth of the outer bubbles inward (VGD8, Figure 2b).

2. At values of $P_f < 6$ MPa a distinct bubble-free core was only observed in short nucleation experiments, with t less than a few tens of seconds (e.g., VGD21, 13 s at P_f = 0.1 MPa; Figure 9a). Longer duration experiments gave rise to complex pumiceous textures characterized by a very large bulk vesicularity, large bubbles separated by relatively thin glassy walls, and a low bubble number density (e.g., VGD12, 300 s at P_f = 0.1 MPa; Figure 9b). A transition from a bubble-free core (VGD13; t = 5 min) to a wholly vesiculated texture (VGD27; t = 30 min) was also observed at P_f = 10 MPa, albeit on a larger timescale. At present, we cannot decisively exclude that the development of these textures was related to some extent to homogeneous bubble nucleation. The low bubble number density in the pumiceous textures and the fact that a bubble-free core was found in a sample held 13 s at 0.1 MPa (Figure 9a) suggest, however, that homogeneous bubble nucleation did not occur even at the lowest values of P_f. Our preferred interpretation is that owing to the very large specific volume of water at low pressure the diffusive and decompressive growth of bubbles nucleated on the platinum wall induced a much larger volume expansion of the external part of the sample at pressures of a few megapascals to 0.1 MPa than at pressures >10 MPa. Owing to this very large expansion

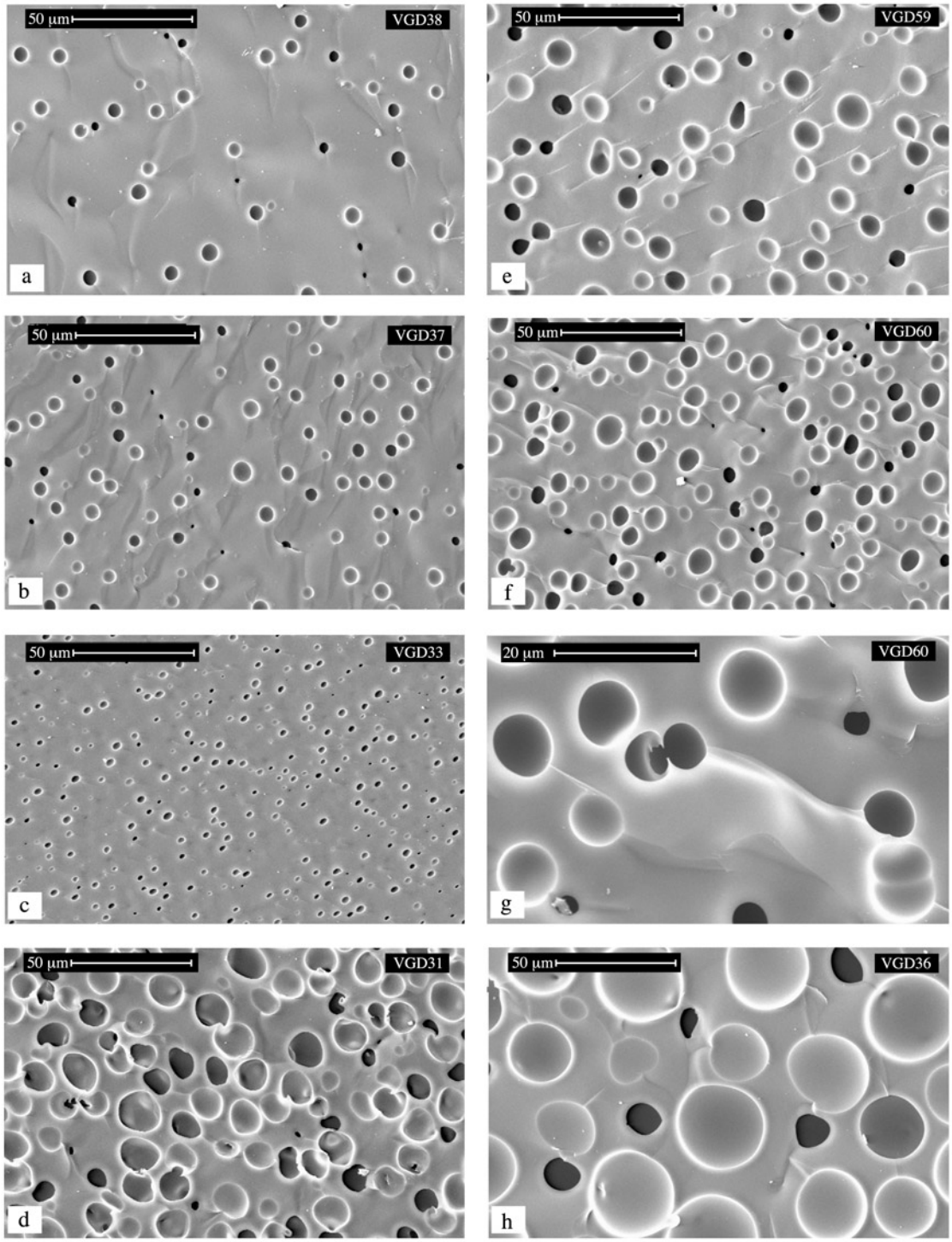

Figure 5. Scanning electron micrographs showing the effect of pressure P_f and duration t of the nucleation step on bubble number density and bubble size in glass type H7C/Ni. (a) VGD38 (P_f = 198 MPa, t = 120 s), (b) VGD37 (P_f = 150 MPa, t = 120 s), (c) VGD33 (P_f = 141 MPa, t = 121 s), (d) VGD31 (P_f = 51 MPa, t = 122 s), (e) VGD59 (P_f = 100 MPa, t = 121 s), (f and g) VGD60 (P_f = 99 MPa, t = 2.5 s; note the abundant quenched coalescing bubbles) and (h) VGD36 (P_f = 50 MPa, t = 90 min).

Table 5. Homogeneous Bubble Nucleation Statistics[a]

Sample	V, vol %	N, m^{-3}	d, μm	σ_d, μm	τ_{Diff},[b] s	t^*,[c] s	N,[d] m^{-3} s^{-1}
H5C/Ni							
VGD42	13.8	5.4×10^{14}	7.4	2.7	58.0	123.4	9.3×10^{12}
VGD41	36.0	3.2×10^{13}	28.5	6.7	381.8	125.5	2.5×10^{11}
VGD53	55.7	4.2×10^{14}	14.2	4.7	68.6	128.6	6.1×10^{12}
H5C/Cu							
VGD62[e]	3.2	5×10^{10}	102	27.1	28354.9	120.4	4.2×10^{8}
H7C/Ni							
VGD39[f]	n.d.	$\approx 10^{11}$	≈85	n.d.	2551.8	121.0	8.3×10^{8}
VGD38	2.9	1.2×10^{14}	6.9	2.6	22.6	123.0	5.3×10^{12}
VGD37	6.3	3.4×10^{14}	5.7	1.6	11.3	127.7	3.0×10^{13}
VGD61	5.0	2.5×10^{14}	6.6	1.6	13.9	10.5	2.4×10^{13}
VGD33	5.0	3.1×10^{15}	2.4	0.7	2.6	134.2	1.2×10^{15}
VGD59	16.8	2.6×10^{14}	9.8	2.9	13.5	137.3	1.9×10^{13}
VGD60	21.0	5.4×10^{14}	8.6	2.3	8.3	19.7	6.5×10^{13}
VGD31	33.9	3.8×10^{14}	10.9	3.9	10.5	140.4	3.6×10^{13}
VGD36	37.1	5.5×10^{13}	21.5	9.0	38.0	5406.9	1.4×10^{12}
H7C/Cu							
VGD52	1.4	8.3×10^{12}	13.9	5.7	134.1	126.2	6.6×10^{10}
VGD45	1.3	2.7×10^{13}	8.6	2.5	61.1	135.1	4.4×10^{11}
VGD44	2.4	6.3×10^{13}	7.9	2.6	34.7	133.4	1.8×10^{12}
VGD43	14.8	7.0×10^{15}	2.8	0.9	1.5	131.4	4.7×10^{15}
VGD63	23.2	7.5×10^{14}	7.5	1.9	6.7	153.9	1.1×10^{14}
H8							
VGD66	3.3	3.8×10^{12}	26.9	7.0	39.5	141.0	9.6×10^{10}
VGD65	7.3	1.2×10^{13}	22.0	7.1	18.4	180.0	6.5×10^{11}
VGD64	25.7	3.9×10^{13}	22.3	7.0	8.4	242.0	4.7×10^{12}

[a] The vesicularity V, bubble number density per unit volume of glass N, mean bubble size d, and the standard deviation of the bubble size distribution σ_d in the core of homogeneously nucleated samples were determined by image analysis of SEM photographs. The errors are 10–20% relative for V, and <10% relative for N and d.

[b] Diffusion timescales τ_{Diff} are computed using (8) and the following values of diffusivities: 1.0×10^{-12} m^2 s^{-1} for glass types H5C/Ni and H5C/Cu (carbon dioxide diffusivity in a rhyolitic liquid at 800°C and 4.5 wt % H_2O [*Watson*, 1991]); 7.0×10^{-12} m^2 s^{-1} for glass types H7C/Ni and H7C/Cu (carbon dioxide diffusivity in a rhyolitic liquid at 800°C and 7 wt % H_2O [*Watson*, 1991); and 4×10^{-11} m^2 s^{-1} for glass type H8 (water diffusivity in a rhyolitic liquid with 8 wt % H_2O).

[c] Here t^* is the total time available for nucleation: it is equal to t plus the part of t_D during which pressure was lower than P_{HoN}.

[d] Average nucleation rates computed using (9a) and (9b).

[e] The vesicularity and the bubble number density of VGD62 were estimated directly under a petrographic microscope by measuring the diameter of 15 bubbles (for a total of 16) and the volume of the nucleated core.

[f] N and d were not measured directly in sample VGD39. The estimates quoted were inferred from the textural analogy of samples VGD39 and VGD62, as follows: (1) N in VGD39 was set equal to twice the bubble number density in VGD62 because its number of bubbles is twice, and (2) d was computed using the equation $\pi N d^3/6 = 0.032$, where the vesicularity of VGD39 was assumed to be equal to that of VGD62 (3.2 vol %).

the core of the sample, which kept its initial water content and therefore had a low viscosity, was stretched and could no longer be identified after only a few tens of seconds.

4. Discussion

4.1. Arguments for the Homogeneous Nature of Bubble Nucleation in Our Experiments

[28] By using bubble- and crystal-free glasses produced by hydration of obsidian solid rods at 1000°C we were able to eliminate at once the problems related to heterogeneous bubble nucleation and to the presence of trapped air bubbles. With these glasses we could lower the pressure much below the saturation pressure without triggering any bubble nucleation except at or close to the contact with the platinum container (Figure 2). In five of the six volatile compositions investigated a transition from a bubble-free core at large values of P_f to a densely nucleated core at lower values of P_f was observed. The unimodal bubble size distributions in the densely nucleated cores suggest a single nucleation event (Figure 10). The main arguments supporting homogeneous bubble nucleation are the following.

1. Bubble nucleation cannot be heterogeneous in the core of the samples because there are no crystals to serve as sites for nucleation either in the starting glass or in the final product at the end of the nucleation experiment. The absence of crystals was checked by optical microscopy and by scanning electron microscopy using both backscattered electron (BSE) imaging of polished sections and secondary electron (SE) imaging of fracture surfaces (microtextural details down to ~200 nm or <100 nm can be detected by BSE and SE imaging, respectively). The absence of crystals in the starting glasses was due to the high temperature of 1000°C at which GDO was hydrated, that is, from 200 to 300°C above the liquidus temperature for water concentrations of 4–8 wt %. Also, in most decompression experiments (those at $P_f \geq 80$ MPa) the run temperature of 800°C was much larger than the liquidus temperature at water saturation [*Simakin et al.*, 1999]. In the nucleation experiments at $P_f \leq 51$ MPa (e.g., VGD62; Figure 7) the run temperature was presumably slightly lower than the liquidus temperature of our obsidian composition, but no crystal was observed because of the long nucleation delay required for crystallization [e.g., *Kirkpatrick*, 1981].

2. A striking feature of the densely nucleated cores and a strong argument for homogeneous bubble nucleation is their textural homogeneity (Figures 4 and 5): no spatial variation of the bubble number density and mean bubble size was detected inside these cores. The textures of the short t experiments (VGD60-61) suggest that the spatial distribution of nuclei was random: in sample VGD60 (P_f = 99 MPa, t = 2.5 s), the nuclei center-to-center distances ranged from only a few micrometers (for the

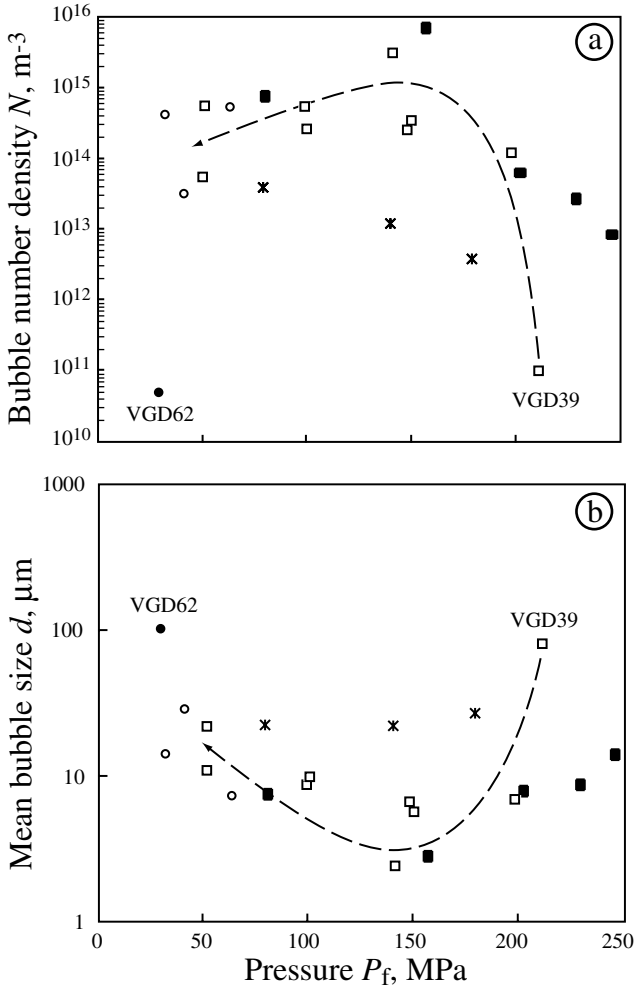

Figure 6. Plot of (a) bubble number density and (b) mean bubble size as a function of the pressure of the nucleation step P_f for compositions H7C/Ni (open squares), H7C/Cu (solid squares), H5C/Ni (open circles), H5C/Cu (solid circles), and H8 (stars). The dashed lines indicate the trends followed by H7C/Ni composition. The pressure P_f in experiments VGD39 and VGD62 is interpreted to be just slightly lower (by a few megapascals or less) than the critical pressure of nucleation of glass type H7C/Ni and H5C/Cu, respectively, because of their very low bubble number densities and their abnormally large mean bubble sizes.

coalescing bubbles) to 10–20 μm for most bubbles (Figures 5f and 5g), and bubble-free domains up to 50 μm in size were also present. By comparison, the spatial distribution of bubbles in VGD59 (P_f = 100 MPa, $t \approx$ 121 s; Figure 5e) is more uniform because the bubbles that nucleated close to one another have coalesced.

3. The very large degrees of supersaturation required for bubble nucleation in our experiments and the strong increase of bubble number density with decreasing P_f in glasses H7C/Ni and H7C/Cu (four orders of magnitude for t = 2 min and P_f from 211 to 141 MPa; Figure 6a) are in agreement with the predictions of classical theory of homogeneous bubble nucleation. In particular, the degrees of supersaturation required for bubble nucleation in the core of our samples (≈60–310 MPa depending on glass type; see section 4.4) are much larger than the critical degrees of supersaturation measured in the case of heterogeneous bubble nucleation (a few megapascals to a few tens of megapascal [*Hurwitz and Navon*, 1994]).

4.2. Homogeneous Bubble Nucleation: Theoretical Aspects

[29] Homogeneous bubble nucleation is defined as the formation of bubbles in a liquid far from any solid particles or impurities. Since the nineteenth century, this phenomenon has been formalized in what is now known as the classical theory [*Hirth et al.*, 1970; *Sparks*, 1978; *Bottinga and Javoy*, 1990; *Hurwitz and Navon*, 1994; *Debenedetti*, 1996]. In classical theory, homogeneous bubble nucleation is assumed to start with the formation of small clusters of water molecules due to random fluctuations in the liquid. The change of free energy resulting from the formation of a cluster is the sum of two components: a decrease of energy resulting from the phase change (below the saturation pressure the vapor plus liquid phases have a lower total free energy than the supersaturated liquid) and an increase of energy associated with the formation of an interface between the vapor phase and the liquid. The net free energy of formation increases with the cluster size up to a maximum value for a critical size. Above this critical size the net free energy of formation decreases with increasing cluster size so that clusters bigger than the critical size grow spontaneously into bubble nuclei. The nucleation rate is thus the rate of formation of clusters bigger than the critical size. Consequently, bubble nucleation can only proceed if the liquid exceeds a certain degree of supersaturation in volatiles, which can either be expressed in terms of composition [*Bottinga and Javoy*, 1990] or in terms of pressure [*Hurwitz and Navon*, 1994]. In the following discussion the critical degree of supersaturation ΔP_{HoN} is expressed in terms of pressure: $\Delta P_{\mathrm{HoN}} = P_{\mathrm{Sat}} - P_{\mathrm{HoN}}$ and is given by [*Hurwitz and Navon*, 1994]

$$\Delta P_{\mathrm{HoN}} = \sqrt{\frac{16\pi\sigma^3}{3kT\ln(J_o/J)}}, \tag{1}$$

where σ is the surface tension, k is Boltzman constant (k = 1.38 × 10^{-23} J K^{-1}), T is the temperature (in K), J is the nucleation rate (in m^{-3} s$^{-1)}$, and J_o is the preexponential nucleation rate (in m^{-3} s^{-1}). The coefficient J_o is derived as follows [*Hurwitz and Navon*, 1994]:

$$J_o = \frac{2\Omega_L n_o^2 D}{a_o}\sqrt{\frac{\sigma}{kT}}, \tag{2}$$

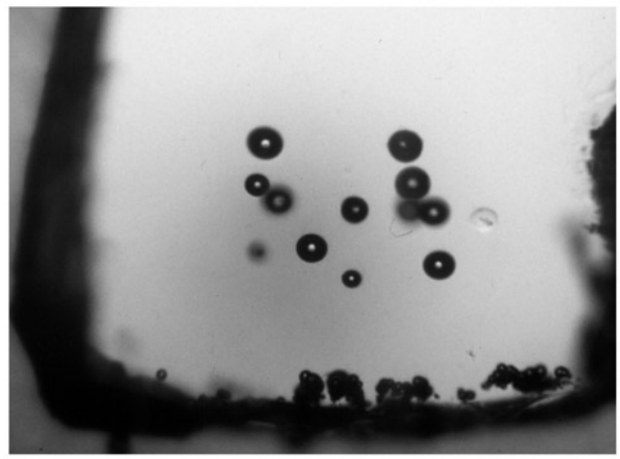

Figure 7. Photomicrograph of the lower two thirds of sample VGD62 showing a core comprising a very small number of large bubbles and a population of small bubbles formed by heterogeneous nucleation on the capsule walls. The field of view is 2.1 mm long.

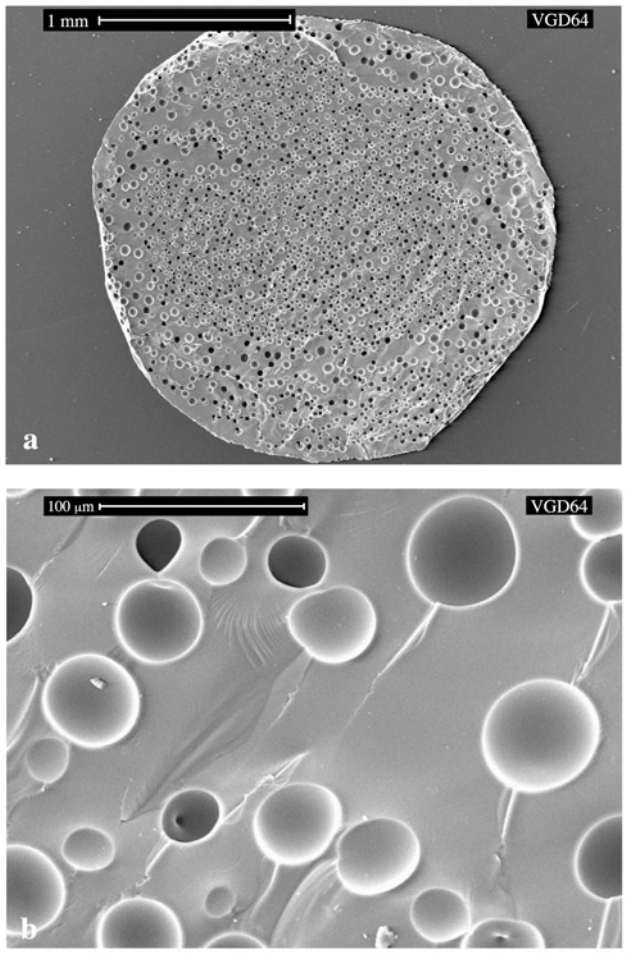

Figure 8. Scanning electron micrographs of a fracture surface of sample VGD64 (glass type H8; P_f = 79 MPa, t = 121 s). (a) Overall view and (b) close-up of the core texture to be compared with Figures 5a–5d.

where Ω_L is the volume of volatile molecules in the liquid, n_o is the number of volatile molecules in the liquid per unit volume, D is the diffusion coefficient, and a_o is the mean distance between volatile molecules in the melt. In the calculation of ΔP_{HoN} an arbitrary value of nucleation rate J is generally assumed, inducing a minor error on the result. The nucleation rate can, however, vary by several orders of magnitude in magmas and is classically expressed as the product of the dimensionless Zeldovitch factor Z, the frequency ω of formation of nuclei with a size bigger than the critical value, and the concentration of growing nuclei n^*. The Zeldovitch factor and the frequency ω are respectively written [*Hirth et al.*, 1970; *Hurwitz and Navon*, 1994]

$$Z = \frac{\Omega_L \Delta P^2}{8\pi\sigma^{1.5}\sqrt{kT}} \tag{3}$$

$$\omega = \frac{16\pi\sigma^2 n_o D}{a_o \Delta P^2}, \tag{4}$$

where ΔP is the pressure drop compared to saturation pressure. The resulting nucleation rate is given as [*Hurwitz and Navon*, 1994]

$$J = J_o e^{-\left(16\pi\sigma^3/3kT\Delta P^2\right)}. \tag{5}$$

Additionally, the bubble nucleation delay τ (that is, the lag time for the establishment of a steady state concentration of critical nuclei) can be derived from [*Debenedetti*, 1996]

$$\tau = \frac{1}{4\pi}\frac{1}{\omega Z^2}. \tag{6}$$

Let us now consider a rhyolitic magma containing 4.5 wt % water. The number of water molecules per unit volume is $n_o = 3.4 \times 10^{27}$ m^{-3}, and the distance between molecule centers is $a_o = {n_o}^{-1/3} = 6.65 \times 10^{-10}$ m. Taking a temperature T of 800°C, a molecular volume of water of $\Omega_L = 10^{-29}$ m^3, a diffusion coefficient for water of $D = 10^{-11}$ m^2 s^{-1}, a surface tension $\sigma = 0.14$ N m^{-1} (at 150 MPa saturation pressure [*Bagdassarov et al.*, 2000]), we derive a coefficient $J_o = 1.07 \times 10^{34}$ m^{-3} s^{-1}. Assuming a nucleation rate of $J = 10^9$ m^{-3} s^{-1}, the critical degree of supersaturation ΔP_{HoN} equals 232 MPa, and the nucleation delay τ equals 7.5 μs.

[30] An important aspect that is not taken into account in (1)–(6) is the competition between bubble growth and nucleation. In a numerical study of bubble nucleation and growth in a viscous magma ascending at a constant velocity, *Toramaru* [1995] predicted that nucleation events have a short duration and comprise two steps: a first step during which the nucleation rate increases with decreasing pressure in agreement with (5) and a second step during which the nucleation rate rapidly drops to zero. The rapid decrease of the nucleation rate is due to diffusive bubble growth, which reduces the degree of volatile supersaturation and therefore prohibits further nucleation [*Murase and McBirney*, 1973].

4.3. Insights Into the Timing and Duration of the Nucleation Event

[31] The evolutions of bubble number density N and mean bubble size d as a function of pressure P_f are shown in Figure 6 (note that N is the number of bubbles per unit volume of liquid not per unit volume of liquid and bubbles: it is therefore a direct measurement of the number of nuclei formed per unit volume of liquid). The most complete data correspond to the two series of nucleation experiments made with glass types H7C/Ni and H7C/Cu. For these two series the evolution of N and d with decreasing P_f may be subdivided in a high-P_f trend and a low-P_f one. The high-P_f trend is characterized by a large increase of N (up to four orders of magnitude; Table 5) with decreasing P_f. The increase of N is accompanied by a decrease of d. At values of $P_f \leq 100$ MPa the evolution with decreasing P_f is characterized by a slight decrease of N (by ~1 order of magnitude or less) and an increase of d. The physical meaning of these trends and the implications for the timing and duration of the nucleation event and for the nucleation rates involved are discussed below.

4.3.1. Beginning of the nucleation event. [32] We emphasize that nucleation began early, that is, during the decompression step when the pressure dropped below the critical value P_{HoN}. This critical value is not known exactly but is supposed to be slightly larger than 211 MPa for composition H7C/Ni and to lie between 246 and 285 MPa for composition H7C/Cu. The first argument for early nucleation is theoretical: the bubble nucleation delay in a hydrous rhyolitic liquid is only of a few microseconds, so bubble nucleation should proceed during decompression as soon as P_{HoN} is crossed. The second argument is experimental and relies on the high bubble number densities measured in runs VGD61 and VGD60 of short duration t. The fact that N is only slightly lower in VGD61 ($N = 2.5 \times 10^{14}$ m^{-3}, P_f = 148 MPa, t = 1 s) than in VGD37 ($N = 3.4 \times 10^{14}$ m^{-1}, P_f = 150 MPa, t = 120 s) suggests that at P_f = 150 MPa most bubbles nucleated during decompression not during the step at P_f.

4.3.2. Duration of the nucleation event and nucleation rates. [33] It is possible to estimate the duration of the nucleation event in our experiments as follows. Let us consider a unit volume of supersaturated liquid containing N bubble nuclei.

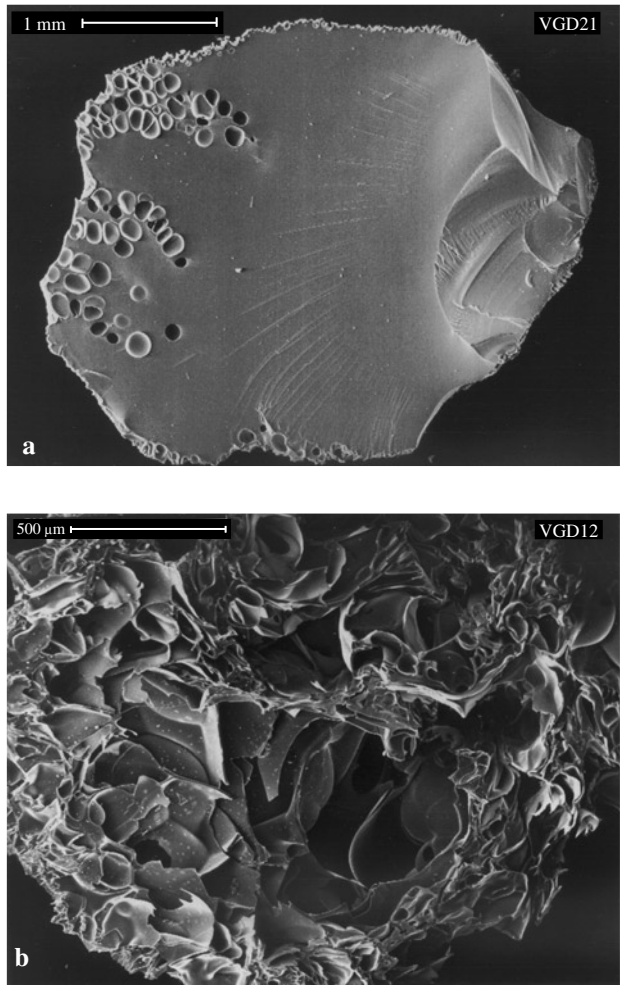

Figure 9. Scanning electron micrographs of fracture surfaces of samples VGD21 and VGD12 (glass type H5). (a) Overall view of sample VGD21 (P_f = 0.1 MPa, t = 13 s) showing a bubble-free core and bubble plumes (on the bottom side of the capsule). (b) Overall view of sample VGD12 (P_f = 0.1 MPa, t = 300 s) showing a pumiceous texture with a large vesicularity and a low number density of large bubbles.

We define τ_{Diff} as the time required for the system to evolve from the supersaturated state to the equilibrium state at the pressure and temperature of interest only by diffusion of volatiles toward the existing bubble nuclei (that is, the number of nuclei per unit volume of liquid is fixed). Clearly, the larger the number of nuclei, the shorter the average distance between neighboring nuclei and the smaller the diffusion timescale τ_{Diff}. To compute τ_{Diff}, we assume that the N nuclei are uniformly spaced so that a volume of liquid equal to N^{-1} is associated to each nucleus. In first approximation we assumed that this volume is a sphere of radius S [e.g., *Navon and Lyakhovsky*, 1998]:

$$S = \left(\frac{3}{4\pi N}\right)^{1/3}. \tag{7}$$

For the case of pure water the equations giving the equilibrium radius of a bubble located at the center of the sphere of radius S as well as the time required to attain this equilibrium radius as a function of the pressure are available [*Navon and Lyakhovsky*, 1998]. Two main volatile components, H_2O and CO_2, were present in our experiments, and we approximated τ_{Diff} by the time required for the diffusion of the volatiles contained in the sphere of radius S to the central nucleus:

$$\tau_{\mathrm{Diff}} = \frac{S^2}{D} = \frac{1}{D}\left(\frac{3}{4\pi N}\right)^{2/3}. \tag{8}$$

Note that, as such, τ_{Diff} is a minimum value for the diffusion timescale because it is based on the final bubble number density. The composition of bubbles in glasses H7C/Ni and H7C/Cu is dominated by CO_2 (~80 mol % CO_2 in VGD38, VGD45, and VGD44, as determined by micro-Raman spectrometry at Centre de Recherches sur la Géologie de l'Uranium (CREGU), Nancy). Carbon dioxide diffusivity in a rhyolitic liquid is strongly sensitive to the content of dissolved water and is $\sim 7 \times 10^{-12}$ $\mathrm{m}^2\ \mathrm{s}^{-1}$ at 800°C and 7 wt % H_2O [*Watson*, 1991]. Using this

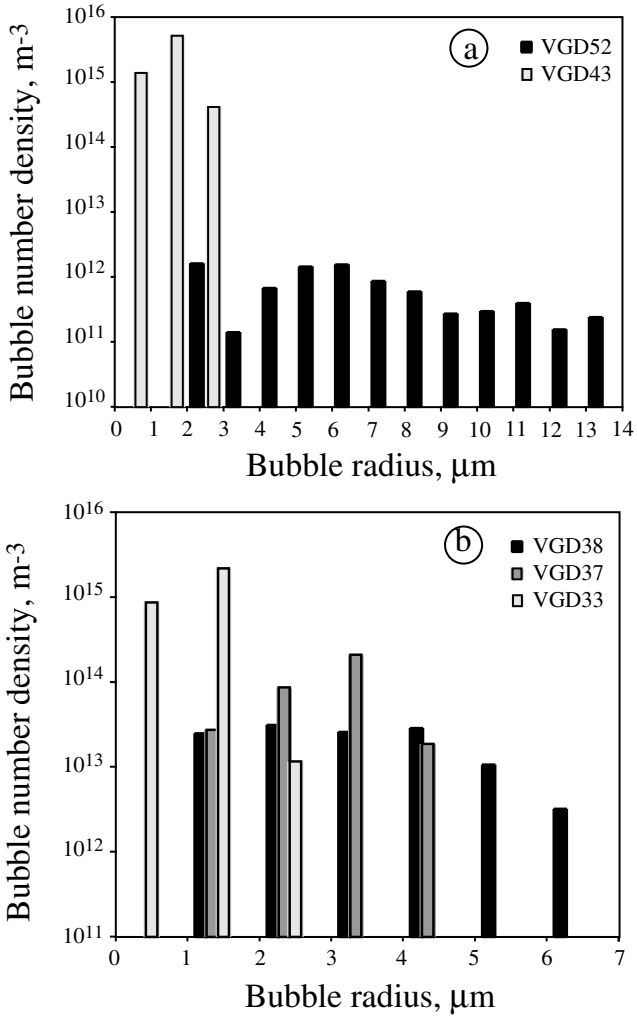

Figure 10. Bubble size distributions in selected samples. (a) Series H7C/Cu: VGD52 (P_f = 246 MPa, $N = 8.3 \times 10^{12}$ m^{-3}) and VGD43 (P_f = 157 MPa, $N = 7.0 \times 10^{15}$ m^{-3}). (b) Series H7C/Ni: VGD38 (P_f = 198 MPa, $N = 1.2 \times 10^{14}$ m^{-3}), VGD37 (P_f = 150 MPa, $N = 7.0 \times 10^{15}$ m^{-3}), and VGD33 (P_f = 141 MPa, $N = 3.1 \times 10^{15}$ m^{-3}).

value of diffusivity in (8), we computed τ_{Diff}, and we compared the results to the total time available for bubble nucleation and growth, t^*, defined as the sum of t plus the part of the decompression duration t_D during which pressure was lower than P_{HoN} (Table 5). The following results emerge.

1. In the few experiments with a low bubble number density, such as VGD52 or VGD39, one has $\tau_{\text{Diff}} > t^*$. In these experiments the average distance between neighboring nuclei was too large for the equilibrium state to be reached by diffusive bubble growth in the time interval t^*. Consequently, bubble nucleation presumably continued during the whole nucleation step (although at a decreasing rate owing to the decreasing degree of supersaturation). A good argument for a protracted nucleation event in VGD52 is the relatively large bubble size distribution (Figure 10a), the larger bubbles having nucleated at the beginning of the nucleation step or even during decompression and the smaller bubbles forming at the end of the nucleation step.

2. The calculation of a timescale τ_{Diff} just slightly longer than t^* in VGD61 (13.4 versus 10.5 s) is in good agreement with the textural observations. Comparing the bubble number densities in samples VGD61 and VGD37, we concluded that at P_f = 150 MPa most of the nucleation occurred during decompression and that the nucleation event was almost terminated in sample VGD61. This good agreement suggests that τ_{Diff} is a good proxy for the duration of the nucleation event in the experiments with $\tau_{\text{Diff}} \leq t^*$.

3. In most experiments the bubble number density is so large that $\tau_{\text{Diff}} < t^*$ (Table 5). In compositions H7C/Cu, for instance, τ_{Diff} is shorter than t^* for all experiments except VGD52. In sample VGD43 the bubble number density is at a maximum ($N = 7.0 \times 10^{15}$ m^{-3}), and τ_{Diff} is as short as 1.4 s. We also observe a continuous evolution of bubble size distribution with decreasing τ_{Diff} from a broad distribution with a large mean size (VGD52, d = 13.9 μm, σ_d = 5.7 μm) to a very narrow distribution with a very small mean size (VGD43, d = 2.8 μm, σ_d = 0.9 μm; Figure 10a). A similar evolution is displayed in Figure 10b for series H7C/Ni. The best explanation for the extreme textural features of sample VGD43 is a very short nucleation event with enormous nucleation rates giving rise to a huge number density of equal-sized bubbles. As a consequence of the very short average distance between neighboring nuclei, diffusive bubble growth resulted in an ultrafast decrease of the degree of supersaturation (over a timescale of 1 s) and nucleation presumably stopped even before the end of the decompression step. The very small mean bubble size in VGD43 is a direct consequence of the huge bubble number density: in a system with $N = 7.0 \times 10^{15}$ m^{-3} and an equilibrium vesicularity of 15 vol %, the equilibrium bubble size is only ≈3 μm.

[34] For the experiments with $\tau_{\text{Diff}} > t^*$, the duration of the nucleation event may be approximated by t^*, and the average nucleation rate is

$$\dot{N} \approx \frac{N}{t^*} (\tau_{\text{Diff}} > t^*). \tag{9a}$$

In the experiments with $\tau_{\text{Diff}} < t^*$ the nucleation event may be much shorter than t^*, and a better approximation of the duration of the nucleation event is provided by the diffusion timescale τ_{Diff}. The average nucleation rate is then

$$\dot{N} \approx \frac{N}{\tau_{\text{Diff}}} (\tau_{\text{Diff}} < t^*) \tag{9b}$$

(as τ_{Diff} is computed using the final value of N, it gives a minimum value for the diffusion timescale, and (9b) gives a maximum estimate for the average nucleation rate). Using (9a) and (9b), we obtained nucleation rates ranging from $10^8 - 10^{10}$ m^{-3} s^{-1} for the lower values of N (VGD39 and VGD52) to $>10^{15}$ m^{-3} s^{-1} for the larger values of N (VGD33 and VGD43; Table5). This huge increase of the nucleation rate with decreasing pressure P_f is in agreement with the qualitative behavior inherent to classical theory of bubble nucleation.

4.3.3. Importance of coalescence at low values of P_f. [35] The N versus P_f plot in Figure 6 shows a very distinct reversal of the evolutionary trend somewhere between 140 and 100 MPa. It is difficult to explain the lower values of N at $P_f \leq 100$ MPa by a decreased average nucleation rate. A more simple explanation is that during decompression, N first increased rapidly and then began to decrease because of the effect of bubble coalescence. The experimental textures indicate that coalescence may operate during the nucleation stage even at a moderately low vesicularity (20 vol % or less) because of the random spatial distribution of bubble nuclei: the nuclei may form so close to one another that they rapidly impinge on one another during their subsequent growth. The large number of quenched coalescence events in VGD60 (P_f = 99 MPa, t = 2.5 s; Figures 5 and 5g) provides very strong evidence for the importance of early bubble coalescence at low P_f. We presume that the coalescence rate was negligible at large values of P_f and that at $P_f \leq 100$ MPa it rapidly

Table 6. Summary of Saturation, Nucleation and Critical Degrees of Supersaturation[a]

	H5	H5C/Ni	H5C/Cu	H7C/Cu	H7C/Ni	H8
H_2O[b]	4.1	4.6	4.6	7.0	7.0	7.7
CO_2[b]	50	800	1100	480	630	10
P_{Sat}[c]	135	288 (±24)	342 (±33)	326 (±14)	353 (±19)	268
P_{HoN}[d]	≤0.1	63–101	29	246–285	211	201-220
ΔP_{HoN}	≥135	163–249	280–346	27–94	123–161	48-67

[a] The saturation pressures P_{Sat}, nucleation pressures P_{HoN}, and critical degree of supersaturation ΔP_{HoN} are given in MPa.

[b] The values listed for H_2O (wt %) and CO_2 (ppm) correspond to the most critical experiments (those that bracket the nucleation pressure; Tables 2 and 3).

[c] All saturation pressures are given at 800°C. The following assumptions are made to compute P_{Sat}: (1) for a given amount of dissolved H_2O, the effect of dissolved CO_2 is to increase P_{Sat} by 18 ± 3 MPa per 100 ppm added CO_2 [*Blank et al.*, 1993; *Wallace et al.*, 1995; *Tamic et al.*, 2001]; (2) in the absence of CO_2 the saturation pressure of our obsidian composition equals 141 MPa for 4.5 wt % dissolved H_2O (estimated from the data for saturation runs H5-8, H5-9, and H5-11, taking in account the effect of dissolved CO_2) and 280 MPa for 8.0 wt % dissolved H_2O (estimated from the water content in glass H8 water saturated at 280 MPa and 1000°C, taking in account a slight increase of water solubility with decreasing temperature [*Holtz et al.*, 1992]); and (3) water solubility increases linearly between 150 and 280 MPa [*Silver et al.*, 1990]. The saturation pressures listed for compositions H5 and H8 are slightly lower than the pressures of the saturation experiments H5-5 and H5-6 (150 MPa) and H8-17 (280 MPa) because of the 200°C temperature difference between the saturation and the decompression experiments.

[d] For series H5C/Ni, H7C/Cu, and H8, P_{HoN} is bracketed by the maximum value of P_f at which an homogeneous nucleation texture was produced and the minimum value of P_f at which a bubble-free core was obtained. The lower bracket of P_{HoN} in series H8 is based on an unpublished experiment [*Laporte et al.*, 2000] in which an homogeneous nucleation texture was obtained at P_f = 201 MPa (and a decompression rate of 10 MPa h^{-1}). For composition H5, homogeneous nucleation was not observed even at P_f = 0.1 MPa. For compositions H5C/Cu and H7C/Ni the pressure P_f in runs VGD62 and VGD39, respectively, is considered to be just slightly lower than P_{HoN} as indicated by the very low bubble number densities.

increased with decreasing pressure due to increasing bubble number density and increasing vesicularity.

[36] Owing to the effect of early coalescence on bubble number density the calculations of τ_{Diff} and of the average nucleation rate in the experiments at low P_f (VGD59, VGD60, VGD31, and VGD36 in composition H7C/Ni and VGD63 in composition H7C/Cu; Table 5) are strongly biased: the diffusion timescale is overestimated, and the average nucleation rate computed using (9b) is underestimated. However, the relationship $\tau_{Diff} < t^*$ is always satisfied, showing that chemical equilibrium was rapidly approached in these experiments. Therefore the reversal in the d versus P_f plot at low P_f results from a combination of decreased bubble number densities (due to coalescence) and increased vesicularities (due to lower values of P_f).

4.3.4. Nucleation parameters in glasses H5C/Ni, H5C/Cu, and H8. [37] The diffusion timescales and the nucleation rates for glass types H5C/Ni, H5C/Cu, and H8 are reported in Table 5. Sample VGD62 (glass type H5C/Cu) provides the best example of a case in which the nucleation event was not terminated at the end of the interval at pressure P_f. The very small total number of bubbles, 16, and the large bubble size distribution, from 34 to 135 μm, argue for a protracted nucleation event and an extremely low average nucleation rate.

[38] The three experiments made with glasses H8 define a trend of increasing N with decreasing P_f. Despite similar nucleation pressures the bubble number densities in these experiments are lower by 1–2 orders of magnitude than those measured in glasses H7C/Ni or H7C/Cu, and the mean bubble size is much larger (25 μm). For the computation of diffusion timescales in a liquid with 7.7 wt % dissolved H_2O, we used a water diffusivity of 4×10^{-11} m^2 s^{-1}, slightly larger than the value proposed for a rhyolitic liquid with 5 wt % H_2O by *Lyakhovsky et al.* [1996]. The diffusion timescales obtained are all clearly shorter than t^*, indicating that nucleation stopped before the end of the experiment (Table 5). The average nucleation rates range from 9.6×10^{10} m^{-3} s^{-1} in VGD66 (P_f = 179 MPa) to 4.7×10^{12} m^{-3} s^{-1} in VGD64 (P_f = 79 MPa).

4.4. Volatile Supersaturation Pressures ΔP_{HoN} Required for Homogeneous Nucleation

[39] Saturation pressures, nucleation pressures, and the values of ΔP_{HoN} for the six volatile compositions studied are summarized in Table 6. There is a considerable uncertainty on saturation pressures (and thus on ΔP_{HoN}), especially for the CO_2-rich compositions because the solubility of mixed H_2O-CO_2 fluids in rhyolitic liquids is still insufficiently constrained [*Blank et al.*, 1993; *Holloway and Blank*, 1994; *Nabelek and Ternes*, 1997; *Papale*, 1999; *Tamic et al.*, 2001]. Whatsoever the uncertainty, the pressures summarized in Table 6 point to several important effects.

1. The degree of supersaturation required for homogeneous bubble nucleation decreases with increasing water content. In the CO_2-poor compositions, ΔP_{HoN} decreases from a value ≥135 MPa at 4.1 wt % H_2O (series H5) to ≈60 MPa at 7.7 wt % H_2O (series H8). These values are in good agreement with the value of 120 MPa measured by *Mangan and Sisson* [2000] for a rhyolite composition with 5.2 wt % H_2O. A straightforward explanation to this effect is that the rhyolite-water surface tension decreases with increasing water content in the rhyolitic liquid [*Bagdassarov et al.*, 2000]. We used (1) to compute the values of surface tensions corresponding to the measured ΔP_{HoN}: ≥96 mN m^{-1} in H5 series and in the range 47–60 mN m^{-1} in H8 series; these values are in agreement with the surface tensions measured by *Epel'baum et al.* [1973] and *Khitarov et al.* [1979] but are slightly lower than the values reported by *Bagdassarov et al.* [2000].

2. Carbon dioxide has a complex effect on the nucleation pressure because both P_{Sat} and ΔP_{HoN} are strongly dependent on CO_2 (Table 6 and Figure 11). In this paragraph, as in Table 6, the CO_2 contents quoted are those in the most critical nucleation experiments not the mean CO_2 contents given in section 2.1. For a given water content, ΔP_{HoN} increases with increasing CO_2 content: from ≈60 MPa in series H7C/Cu, at 480 ppm CO_2, to ≈140 MPa in series H7C/Ni, at 630 ppm CO_2; from ≈210 MPa in series H5C/Ni, at 800 ppm CO_2, ≈310 MPa in series H5C/Cu, at 1100 ppm CO_2. The effect of carbon dioxide seems to become really important only at very large CO_2 contents: for instance, there is no difference in ΔP_{HoN} between series H8 and H7C/Cu, at 10 and 480 ppm CO_2, respectively. The increase of ΔP_{HoN} at large CO_2 contents is interpreted to be due to an increase of rhyolite surface tension in the presence of a mixed H_2O-CO_2 fluid phase. Dihedral angle measurements for H_2O-CO_2 fluids in polycrystalline aggregates of quartz and olivine [*Watson and Brenan*, 1987; *Holness*, 1992] indicate that the crystalline silicate-fluid interfacial energy increases with increasing molar percentage of CO_2 in the fluid phase. We suggest that a similar relationship exists for molten silicates.

3. An important evolution of the nucleation behavior is observed over a range of dissolved water contents comparable to the range in preeruptive silicic magmas, typically 4–8 wt %

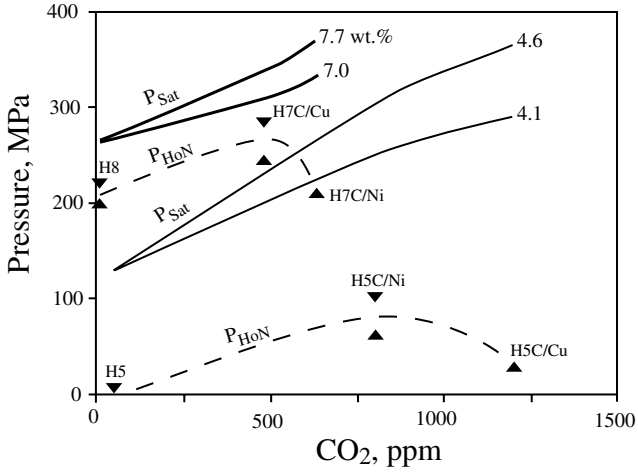

Figure 11. Saturation and nucleation pressures as a function of CO_2 concentration for water contents of 4.1–4.6 wt % H_2O (volatile compositions H5, H5C/Ni, and H5C/Cu) and 7.0–7.7 wt % H_2O (volatile compositions H8, H7C/Ni, and H7C/Cu). The nucleation pressures are shown by the dashed lines. The saturation pressures are shown by the solid lines (thick lines are 7.0–7.7 wt % H_2O, and thin lines are 4.1–4.6 wt% H_2O); the solid triangles are the experimental brackets.

(Figure 11) [e.g., *Johnson et al.*, 1994]. Owing to their low saturation pressures and large ΔP_{HoN}, rhyolitic liquids with 4–5 wt % H_2O are expected to have very low nucleation pressures. By contrast, rhyolitic liquids with larger water contents have high nucleation pressures because of a combination of higher saturation pressures and much lower critical degrees of supersaturation. These contrasted nucleation behaviors may possibly lead to major differences in the vesiculation histories of H_2O-poor and H_2O-rich silicic magmas (see section 4.5).

4.5. Volcanological Implications

4.5.1. Importance of homogeneous bubble nucleation in ascending rhyolitic magmas. [40] The high bubble number densities in our decompression experiments, up to 10^{15} m^{-3}, are comparable to the densities measured in natural silicic pumices, 10^{11}–10^{15} m^{-3} [*Whitham and Sparks*, 1986; *Toramaru*, 1990; *Klug and Cashman*, 1994]. This agreement may well be fortuitous, but it suggests to us that homogeneous nucleation is a viable mechanism for the formation of bubbles in rhyolitic magmas. In the presence of phenocrysts or microlites, heterogeneous nucleation of bubbles on crystals may, however, require a significantly lower degree of volatile supersaturation than homogeneous nucleation [*Hurwitz and Navon*, 1994]. An early event of heterogeneous nucleation can prevent large degrees of supersaturation from building up during magma ascent and thus prohibit a late event of homogeneous nucleation. Typical phenocryst number densities are, however, relatively low [*Sparks et al.*, 1994] and should only give rise to a small number of heterogeneously nucleated bubbles. Assuming phenocryst densities $\leq 10^6$ m^{-3}, the average spacing between early nucleated bubbles ($\approx 10^{-2}$ m from (7)) will leave large bubble-free domains where homogeneous nucleation could proceed and yield very high bubble number densities. *Hammer et al.*'s [1999] measurements in Pinatubo dacite suggest that the number density of microlites may reach 10^{16} m^{-3}. Therefore the development of a population of microlites, in particular Fe-Ti oxide microlites [*Hurwitz and Navon*, 1994], can strongly favor heterogeneous bubble nucleation to the expense of homogeneous nucleation. However, the crystallization of microlites during magma ascent occurs as a consequence of volatile exsolution [*Swanson et al.*, 1989; *Gerschwind and Rutherford*, 1995], and therefore it cannot affect the early stages of bubble nucleation.

4.5.2. Degrees of supersaturation required for bubble nucleation in ascending magmas. [41] An important contribution of our study is to show that the critical degrees of volatile supersaturation can be much larger than previously anticipated and that they are strongly dependent on H_2O and CO_2 concentrations (Table 6; the data in Table 6 correspond to a single composition, an SiO_2-rich obsidian, and we do not know at present if there is a strong effect of major element composition on ΔP_{HoN}). Knowing the wetting angle of a bubble on a crystal face, it is possible to compute the critical degree of supersaturation required for heterogeneous nucleation, ΔP_{HeN}, from the value of ΔP_{HoN} [*Hurwitz and Navon*, 1994]. The wetting angle θ is defined at the junction of the bubble surface with the crystal face: it is the angle between the crystal face and the tangent to the bubble surface, measured through the silicate liquid. Crystals may serve as efficient sites for heterogeneous nucleation if the surface energy of the crystal-vapor interface is significantly lower than the silicate liquid-vapor interfacial energy, that is, if the wetting angle is large. For instance, the degree of supersaturation required for bubble nucleation on a flat crystal face with $\theta = 150°$ equals only 11% of the degree of supersaturation required for homogeneous nucleation [*Hurwitz and Navon*, 1994; *Navon and Lyakhovsky*, 1998]. For nonwetting bubbles ($\theta < 90°$) the efficiency of heterogeneous bubble nucleation is much lower: the ratio $\Delta P_{HeN}/\Delta P_{HoN}$ equals 0.5 for $\theta = 90°$, 0.99 for $\theta = 30°$, and 1 for perfectly nonwetting bubbles ($\theta = 0°$).

[42] Precise measurements of wetting angles of water bubbles on the major mineral species in silicate magmas are presently not available. The data collected by *Hurwitz and Navon* [1994] suggest that the wetting angles are >90° only for Fe-Ti oxides and biotites. In their experiments, Fe-Ti oxides are by far the most efficient sites for bubble nucleation: extensive bubble nucleation occurred on Fe-Ti oxides only 5 MPa below the volatile saturation pressure (this very low degree of supersaturation was presumably due in part to the rough morphology of Fe-Ti oxide microlites [*Hurwitz and Navon*, 1994]). On the contrary, wetting angles for H_2O-rich bubbles on quartz and plagioclase seem to be very low (0° to a few tens of degrees). We measured the wetting angles of water bubbles on quartz in two of our past experiments (QAn10a and QAn18a [*Laporte*, 1994]): the average wetting angle is 24° in sample QAn10a and 22° in sample QAn18a (based on 10 and 11 apparent angles, respectively). Textural observations on natural samples also suggest that bubbles are nonwetting on plagioclases ($\theta < 20°$ [*Hurwitz and Navon*, 1994]). This very incomplete data set indicates that only a few mineral species are able to promote bubble nucleation at relatively low degrees of supersaturation ($\Delta P_{HeN} \leq \Delta P_{HoN}/2$). Major mineral species such as quartz and plagioclase cannot act as efficient sites of bubble nucleation: for these species, one has $\Delta P_{HeN} \approx \Delta P_{HoN}$. Accordingly, very large degrees of supersaturation (>135–310 MPa for a SiO_2-rich composition with 4.5 wt % dissolved H_2O; Table 6) can build up in a rhyolitic magma during ascent even in the presence of abundant phenocrysts of quartz and plagioclase.

4.5.3. Implications for the dynamics of magma ascent. [43] Our experiments show that the vesiculation of ascending rhyolitic magmas cannot be described satisfactorily by a model of equilibrium degassing assuming a deep bubble nucleation event at a pressure equal to the saturation pressure, followed by a progressive increase of vesicularity with decreasing pressure. For rhyolitic magmas with moderate water contents (4–5 wt % H_2O), a more realistic model should incorporate the following ingredients: (1) the buildup of large degrees of supersaturation due to the absence of bubble nuclei or to an insufficient number of bubbles (in the case of an early event of heterogeneous nucleation), (2) a very late event of homogeneous bubble nucleation occurring at a

shallow level, and (3) an "explosive" vesiculation [*Sparks et al.*, 1994] through which vesicularity may rapidly approach its equilibrium value (because of the low nucleation pressure, the equilibrium vesicularity may be large: >50 or even >70 vol %).

[44] For the second ingredient the very small values of the diffusion timescales τ_{Diff} in most of our experiments (Table 5) suggest that bubble nucleation in ascending magmas must not be considered steady in time. As anticipated by *Toramaru* [1995], the nucleation event is more likely to be short-lived and to comprise a first step during which the nucleation rate rapidly increases with decreasing pressure and a second step during which the nucleation rate drops to zero. The arrest of nucleation is due to the fact that when the average distance between neighboring nuclei is small, diffusive bubble growth can reduce the degree of volatile supersaturation to a sufficiently low level to prohibit further nucleation.

[45] For the third ingredient, explosive vesiculation is made possible by the high bubble number densities associated with homogeneous nucleation. The number density of bubbles at the end of the nucleation event will depend on the ascent rate and must therefore be lower than the maximum values measured in our rapid decompression experiments (the slower the ascent, the lower the bubble number density [*Toramaru*, 1995]). Assuming that a bubble number density of 10^{13} m^{-3} is reached at the end of the nucleation event, then the vesicularity may approach its equilibrium value in a matter of a few tens of seconds to a few minutes, as indicated by the values of τ_{Diff} in Table 5. A detailed model should take in account the fact that melt viscosity increases by several orders of magnitude during vesiculation [e.g., *Dingwell*, 1996] and can result in delayed bubble growth [*Bagdassarov et al.*, 1996].

[46] The model of equilibrium degassing may be more appropriate to the case of rhyolitic liquids with larger water contents (7 wt % H_2O) because the difference between the saturation pressure and the nucleation pressure in these liquids is relatively low (Figure 11). Also, because of the high pressures at which homogeneous nucleation occurs the difference between the equilibrium vesicularity and the actual vesicularity at the onset of nucleation (0 vol % in the absence of an early event of heterogeneous nucleation) must be small: only a few vol % to 10 vol %.

5. Conclusions

[47] The results of our experimental study may be summarized as follows.

1. In five of the six volatile compositions investigated we observed a transition from a bubble-free core at large pressures P_f to a nucleated core at lower values of P_f. This transition resulted from a single event of homogeneous nucleation that yielded a large number density of uniformly spaced bubbles with a unimodal size distribution. With decreasing pressure, bubble number densities increased from $<10^{11}$ m^{-3} (for samples quenched just below the critical nucleation pressure P_{HoN}) to $>10^{15}$ m^{-3}.

2. Two fundamentally different types of nucleation textures may be distinguished. In the experiments run at P_f just slightly below P_{HoN} the average nucleation rate was small (10^8–10^{11} m^{-3} s^{-1}), and the nucleation event was not terminated when the experiment was quenched (that is, the degree of supersaturation was still large); these experiments are characterized by relatively small bubble number densities and a large range of bubble sizes. In the experiments run at P_f well below P_{HoN} the average nucleation rate was very large (up to 5×10^{15} m^{-3} s^{-1}), and nucleation rapidly stopped (after a few seconds to a few tens of seconds) because diffusive bubble growth resulted in a rapid decrease of the degree of volatile supersaturation; experiments in this regime show a huge number of small, equal-sized bubbles.

3. The degree of supersaturation required for homogeneous bubble nucleation is very large and is strongly dependent on the amount of H_2O and CO_2 in the rhyolitic liquid. ΔP_{HoN} increases with decreasing H_2O content or increasing CO_2 content. Huge values of ΔP_{HoN} (>135–310 MPa) are measured in the H_2O-poor compositions (4.1–4.6 wt % H_2O; 50–1100 ppm CO_2); much lower values (≈60–140 MPa) are obtained in the H_2O-rich compositions (7.0–7.7 wt % H_2O; 10–630 ppm CO_2).

4. Our experiments indicate that homogeneous nucleation can be an important mechanism of bubble formation in rhyolitic magmas and that it can give rise to very large bubble number densities as observed in natural silicic pumices. The contrasted nucleation behaviors of H_2O-poor and H_2O-rich silicic magmas may lead to major differences in vesiculation histories and magma ascent dynamics: the large ΔP_{HoN} in liquids with 4–5 wt % H_2O should result in a very late nucleation event and an explosive vesiculation. By contrast, the combination of a large P_{Sat} and a small ΔP_{HoN} in H_2O-rich rhyolitic liquids should favor the nucleation of a high number density of bubbles at great depth in the volcanic conduit and a subsequent near-equilibrium degassing.

[48] To conclude, we believe that our experiments provide important constraints for the understanding of bubble nucleation in silicic magmas and for the modeling of magma ascent dynamics. Major issues such as the effect of rhyolite composition or the effect of ascent rate on the physical parameters of homogeneous bubble nucleation remain unconstrained, however, and should be addressed in future experimental studies.

Notation

a_o	mean distance between volatile molecules in the liquid, m.
d	mean bubble diameter, μm.
D	volatile diffusion coefficient, m^2 s^{-1}.
ΔP	pressure drop below saturation pressure, MPa.
ΔP_{HoN}	critical degree of supersaturation $P_{Sat}-P_{HoN}$, MPa.
J	bubble nucleation rate, m^{-3} s^{-1}.
J_o	preexponential coefficient of the nucleation rate J, m^{-3} s^{-1}.
k	Boltzman constant, J K^{-1}.
N	bubble number density, m^{-3}.
$\dot{N}$	mean bubble nucleation rate, m^{-3} s^{-1}.
n_o	number of volatile molecules per unit volume of liquid, m^{-3}.
n^*	concentration of nuclei bigger than the critical size, m^{-3}.
P_{HoN}	critical pressure of homogeneous bubble nucleation, MPa.
P_i	experimental pressure before decompression, MPa.
P_f	experimental pressure after decompression, MPa.
P_{Sat}	volatile saturation pressure, MPa.
S	radius of the sphere of liquid around bubbles, m.
σ	vapor-liquid surface tension, N m^{-1}.
σ_d	standard deviation in bubble size distribution, μm.
T	temperature, K.
t_h	duration of hydration runs, hours.
t	duration of the experimental step at pressure P_f, s.
t^*	equal to t plus the part of t_D during which the pressure is lower than P_{HoN}, s.
t_D	time for decompression from P_i to P_f, s.
τ	lag time for homogeneous bubble nucleation, s.
τ_{Diff}	timescale for volatile diffusion, s.
ω	frequency of critical bubble nuclei formation, s^{-1}.
Ω_L	volume of volatile molecules in the liquid, m^{-3}.
V	vesicularity, vol %.
Z	Zeldovitch dimensionless factor.

[49] **Acknowledgments.** This work was supported by the Institut National des Sciences de l'Univers (grants 97 PNRN AV-19 and 99 PNRN 15 AV; Programme National des Risques Naturels) and the European Commission. The manuscript benefited from discussions with A. Provost, T. Druitt, and R. S. J. Sparks and from constructive reviews by D. R. Baker, H. Sato, and J. H. Hammer. We also benefited from the technical assistance

of M. Carroll and R. Brooker (FTIR spectroscopy, Bristol, United Kingdom), J. Dubessy (micro-Raman spectrometry, CREGU, Nancy, France) and M. Veschambre (electron probe microanalysis, Clermont-Ferrand, France). Special thanks are owed to F. Maciejak and J.-L. Froger who provided the block of Güney Dagi obsidian. This is INSU-CNRS contribution 261.

References

Anderson, A. T., S. Newman, S. N. Williams, T. H. Druitt, C. Skirius, and E. Stolper, H_2O, CO_2, Cl and gas in plinian and ashflow Bishop rhyolite, *Geology*, *17*, 221–225, 1989.

Ayers, J. C., J. B. Brenan, E. B. Watson, D. A. Wark, and W. G. Minarik, A new capsule technique for hydrothermal experiments using the piston-cylinder apparatus, *Am. Mineral.*, *77*, 1080–1086, 1992.

Bacon, C. R., S. Newman, and E. Stolper, Water, CO_2, Cl, and F in melt inclusions in phenocrysts from 3 Holocene explosive eruptions, Crater Lake, Oregon, *Am. Mineral.*, *77*, 1021–1030, 1992.

Bagdassarov, N., D. B. Dingwell, and M. C. Wilding, Rhyolite magma degassing: An experimental study of melt vesiculation, *Bull. Volcanol.*, *57*, 587–601, 1996.

Bagdassarov, N., A. Dorfman, and D. B. Dingwell, Effect of alkalies, phosphorus, and water on surface tension of haplogranite melts, *Am. Mineral.*, *85*, 33–40, 2000.

Barclay, J., M. R. Carroll, B. F. Houghton, and C. T. N. Wilson, Pre-eruptive volatile content and degassing history of an evolving peralkaline volcano, *J. Volcanol. Geotherm. Res.*, *74*, 74–87, 1996.

Barclay, J., M. J. Rutherford, M. R. Carroll, M. D. Murphy, J. D. Devine, J. Gardner, and R. S. J. Sparks, Experimental phase equilibria constraints on pre-eruptive storage conditions of the Soufriere Hills magma, *Geophys. Res. Lett.*, *25*, 3437–3440, 1998.

Blank, J. G., An experimental investigation of the behavior of carbon dioxide in rhyolitic melt, Ph.D. dissertation, Calif. Inst. of Technol., Pasadena, 1993.

Blank, J. G., E. M. Stolper, and M. R. Carroll, Solubilities of carbon dioxide and water in rhyolitic melt at 850°C and 750 bars, *Earth Planet. Sci. Lett.*, *119*, 27–36, 1993.

Bottinga, Y., and M. Javoy, Mid-ocean ridge basalt degassing: Bubble nucleation, *J. Geophys. Res.*, *95*, 5125–5131, 1990.

Brooker, R., J. R. Holloway, and R. Hervig, Reduction in piston-cylinder experiments: The detection of carbon infiltration into platinum capsules, *Am. Mineral.*, *83*, 985–994, 1998.

Coster, M. and J.-L. Chermant, *Précis d'Analyse d'Images*, pp. 149–152, Presses du CNRS, Paris, 1989.

Debenedetti, P. G., *Metastable Liquids, Concepts and Principles*, 411 pp. Princeton Univ. Press, Princeton, N. J., 1996.

Dingwell, D. B., Volcanic dilemma: Flow or blow?, *Science*, *273*, 1054–1055, 1996.

Druitt, T. H., P. J. Brenchley, Y. E. Gökten, and V. Francaviglia, Late Quaternary rhyolitic eruptions from the Acigöl Complex, central Turkey, *J. Geol. Soc. London*, *152*, 655–667, 1995.

Epel'baum, M. B., I. V. Babashov, and T. P. Salova, Surface tension of felsic magmatic melts at high temperatures and pressures, *Geokhimiya*, *3*, 461–464, 1973.

Gardner, J. E., M. Hilton, and M. R. Carroll, Experimental constraints on degassing of magma: Isothermal bubble growth during continuous decompression from high pressure, *Earth Planet. Sci. Lett.*, *168*, 201–218, 1999.

Gerschwind, C.-H., and M. J. Rutherford, Crystallization of microlites during magma ascent: The fluid mechanics of the 1980–1986 eruptions at Mount St Helens, *Bull. Volcanol.*, *57*, 356–370, 1995.

Hammer, J. E., K. V. Cashman, R. P. Hoblitt, and S. Newman, Degassing and microlite crystallization during pre-climactic events of the 1991 eruption of Mt. Pinatubo, Philippines, *Bull. Volcanol.*, *60*, 355–380, 1999.

Hirth, J. P., G. M. Pound, and G. R. St. Pierre, Bubble nucleation, *Metal. Trans.*, *1*, 939–945, 1970.

Holloway, J. R. and J. G. Blank, Application of experimental results to C-O-H species in natural melts, in *Volatiles in Magmas*, edited by M. R. Carroll and J. R. Holloway, *Rev. Mineral., 30*, 187–230, 1994.

Holness, M. B., Equilibrium dihedral angles in the system quartz-CO_2-H_2O-NaCl at 800°C and 1–15 kbar: The effects of pressure and fluid composition on the permeability of quartzites, *Earth Planet. Sci. Lett.*, *114*, 171–184, 1992.

Holtz, F., H. Behrens, D. B. Dingwell, and R. P. Taylor, Water solubility in aluminosilicate melts of haplogranite composition at 2 kbar, *Chem. Geol.*, *96*, 289–302, 1992.

Hurwitz, S., and O. Navon, Bubble nucleation in rhyolitic melts: Experiments at high pressure, temperature and water content, *Earth Planet. Sci. Lett.*, *122*, 267–280, 1994.

Ihinger, P., The interaction of water with granitic melt, Ph.D. dissertation, Calif. Inst. of Technol., Pasadena, 1991.

Jaupart, C., Physical models of volcanic eruptions, *Chem. Geol.*, *128*, 217–227, 1996.

Johnson, M. C., A. T. Anderson Jr. and M. J. Rutherford, Pre-eruptive volatile contents of magmas, in *Volatiles in Magmas*, edited by M. R. Carroll and J. R. Holloway, *Rev. Mineral.*, *30*, 281–323, 1994.

Khitarov, N. I., Y. B. Lebedev, A. M. Dorfman, and N. S. Bagdassarov, Effects of temperature, pressure, and volatiles on the surface tension of molten basalt, *Geochem. Int.*, *16*, 78–86, 1979.

Kirkpatrick, R. J., Kinetics of crystallization of igneous rocks, in *Kinetics of Geochemical Processes*, edited by A. C. Lasaga and R. J. Kirkpatrick, *Rev. Mineral.*, *8*, 321–396, 1981.

Klug, C., and K. V. Cashman, Vesiculation of May 18, 1980, Mount St Helens magma, *Geology*, *22*, 468–471, 1994.

Lange, R. A., and I. S. E. Carmichael, Densities of Na_2O-K_2O-CaO-MgO-FeO-Fe_2O_3-Al_2O_3-TiO_2-SiO_2 liquids: New measurements and derived partial molar properties, *Geochim. Cosmochim. Acta*, *51*, 2931–2946, 1987.

Laporte, D., Wetting behavior of partial melts during crustal anatexis: The distribution of hydrous silicic melts in polycristalline aggregates of quartz, *Contrib. Mineral. Petrol.*, *116*, 486–499, 1994.

Laporte, D., C. C. Mourtada-Bonnefoi, and P. Cacault, Homogeneous bubble nucleation in a rhyolitic liquid: The effect of magma ascent rate, *J. Conf. Abstr.*, *5*, 62, 2000.

Lowenstern, J. B., Dissolved volatile concentrations in an ore-forming magma, *Geology*, *22*, 893–896, 1994.

Lowenstern, J. B., M. A. Clynne, and T. D. Bullen, Comagmatic A-type granophyre and rhyolite from the Alid volcanic center, Eritrea, Northeast Africa, *J. Petrol.*, *38*, 1707–1721, 1997.

Lyakhovsky, V., S. Hurwitz, and O. Navon, Bubble growth in rhyolitic melts: Experimental and numerical investigation, *Bull. Volcanol.*, *58*, 19–32, 1996.

Mangan, T. M., and K. V. Cashman, The structure of basaltic scoria and reticulite and inferences for vesiculation, foam formation, and fragmentation in lava fountains, *J. Volcanol. Geotherm. Res.*, *73*, 1–18, 1996.

Mangan, M., and T. Sisson, Delayed, disequilibrium degassing in rhyolitic magma: Decompression experiments and implications for explosive volcanism, *Earth Planet. Sci. Lett.*, *183*, 441–455, 2000.

Martel, C., M. Pichavant, J.-L. Bourdier, H. Traineau, F. Holtz, and B. Scaillet, Magma storage conditions and control of eruption regime in silicic volcanoes: Experimental evidence from Mt. Pelée, *Earth Planet. Sci. Lett.*, *156*, 89–99, 1998.

Mourtada-Bonnefoi, C. C., Volcanologie physique: Dynamique thermochimique des chambres magmatiques et vésiculation des magmas rhyolitiques, Ph.D. thesis, 209 pp., Univ. Blaise Pascal de Clermont-Ferrand, Clermont-Ferrand, France, 1998.

Mourtada-Bonnefoi, C. C., and D. Laporte, Experimental study of homogeneous bubble nucleation in rhyolitic magmas, *Geophys. Res. Lett.*, *26*, 3505–3508, 1999.

Murase, T., and A. R. McBirney, Properties of some common igneous rocks and their melts at high temperatures, *Geol. Soc. Am. Bull.*, *84*, 3563–3592, 1973.

Nabelek, P. I., and K. Ternes, Fluid inclusions in the Harney Peak Granite, Black Hills, South Dakota, USA: Implications for solubility and evolution of magmatic volatiles and crystallisation of leucogranite magmas, *Geochim. Cosmochim. Acta*, *61*, 1447–1465, 1997.

Navon, O. and V. Lyakhovsky, Vesiculation processes in silicic magmas, in *The Physics of Explosive Eruptions*, edited by J. S. Gilbert and R. S. J. Sparks, *Geol. Soc. Spec. Publ.*, *145*, 27–50, 1998.

Newman, S., E. M. Stolper, and S. Epstein, Measurement of water in rhyolitic glasses: Calibration of an infrared spectroscopic technique, *Am. Mineral.*, *71*, 1527–1541, 1986.

O'Neil, H. S. C., and M. I. Pownceby, Thermodynamic data from redox reactions at high temperatures, I, An experimental and theoretical assessment of the electrochemical method using stabilized zirconia electrolytes, with revised values from the Fe-FeO, Co-CoO, Ni-NiO and Cu-Cu_2O oxygen buffers, and new data from the W-WO_2 buffer, *Contrib. Mineral. Petrol.*, *114*, 296–314, 1993.

Papale, P., Modeling of the solubility of a two-component H_2O + CO_2 fluid in silicate liquids, *Am. Mineral.*, *84*, 477–492, 1999.

Proussevitch, A. A., and D. L. Sahagian, Dynamics of coupled diffusive and decompressive bubble growth in magmatic systems, *J. Geophys. Res.*, *101*, 17,447–17,455, 1996.

Proussevitch, A. A., and D. L. Sahagian, Dynamics and energetics of bubble growth in magmas: Analytical formulation and numerical modeling, *J. Geophys. Res.*, *103*, 18,223–18,251, 1998.

Saltykov, S. A., Stereology, edited by H. Helias, p. 163, Springer-Verlag, New York, 1967.

Silver, L. A., P. D. Ihinger, and E. Stolper, The influence of bulk composition on the speciation of water in silicate glasses, *Contrib. Mineral. Petrol.*, *104*, 142–162, 1990.

Simakin, A. G., P. Armienti, and M. B. Epel'baum, Coupled degassing and crystallisation study at continuous pressure drop, with application to volcanic bombs, *Bull. Volcanol.*, *61*, 275–287, 1999.

Sparks, R. S. J., The dynamics of bubble formation and growth in magmas: A review and analysis, *J. Volcanol. Geotherm. Res.*, *3*, 1–37, 1978.

Sparks, R. S. J., J. Barclay, C. Jaupart, H. M. Mader and J. C. Phillips, Physical aspects of magma degassing, I, Experimental and theoretical constraints on vesiculation, in *Volatiles in Magmas*, edited by M. R. Carroll and J. R. Holloway, *Rev. Mineral.*, *30*, 413–445, 1994.

Swanson, S. E., M. T. Naney, H. R. Westrich, and J. C. Eichelberger, Crystallization history of Obsidian Dome, Inyo Domes, California, *Bull. Volcanol.*, *51*, 161–176, 1989.

Tamic, N., H. Behrens, and F. Holtz, The solubility of H2O and CO2 in rhyolitic melts in equilibrium with mixed CO_2-H_2O fluid phase, *Chem. Geol.*, *174*, 133–347, 2001.

Toramaru, A., Measurement of bubble size distributions in vesiculated rocks with implications for quantitative estimation of eruption processes, *J. Volcanol. Geotherm. Res.*, *43*, 71–90, 1990.

Toramaru, A., Numerical study of nucleation and growth of bubbles in viscous magmas, *J. Geophys. Res.*, *100*, 1913–1931, 1995.

Wallace, P. J., and T. M. Gerlach, Magmatic vapor source for sulfur dioxide released during volcanic eruptions: Evidence from Mount Pinatubo, *Science*, *265*, 497–499, 1994.

Wallace, P. J., A. T. Anderson Jr., and A. M. Davis, Quantification of pre-eruptive exsolved gas contents in silicic magmas, *Nature*, *377*, 612–616, 1995.

Watson, E. B., Diffusion of dissolved CO_2 and Cl in hydrous silicic to intermediate magmas, *Geochim. Cosmochim. Acta*, *55*, 1897–1902, 1991.

Watson, E. B., and J. M. Brenan, Fluids in the lithosphere, 1, Experimentally determined wetting characteristics of CO_2-H_2O fluids and their implications for fluid transport, host-rock physical properties and fluid inclusion formation, *Earth Planet. Sci. Lett.*, *85*, 497–515, 1987.

Whitham, A. G., and R. S. J. Sparks, Pumice, *Bull. Volcanol.*, *48*, 209–223, 1986.

Woods, A. W., The dynamics of explosive volcanic eruptions, *Rev. Geophys.*, *33*, 495–530, 1995.

D. Laporte and C. C. Mourtada-Bonnefoi, Laboratoire Magmas et Volcans, CNRS, Université Blaise Pascal, Observatoire de Physique du Globe de Clermont-Ferrand, 5 rue Kessler, 63038 Clermont-Ferrand cedex, France. (laporte@opgc.univ-bpclermont.fr; c.mourtada@opgc.univ-bpclermont.fr)